Mineralogy and Petrology (2022) 116:401–427
https://doi.org/10.1007/s00710-022-00791-1

ORIGINAL PAPER

Accessory Cr-spinel from peridotite massifs of the South Urals: morphology, composition and origin

Dmitry E. Saveliev[1] · **Vladimir V. Shilovskikh**[2] · **Darkhan K. Makatov**[3] · **Ruslan A. Gataullin**[4]

Received: 16 December 2021 / Accepted: 2 August 2022 / Published online: 27 August 2022

Abstract

The features of morphology and composition of accessory Cr-spinels from four ophiolitic peridotite massifs of the Southern Urals are considered. Massifs are localized in the Main Uralian Fault zone (Nurali, Mindyak), at its junction with the Sakmar zone (Kempirsai) and in the northern part of the Zilair zone (Kraka). The Kraka, Nurali and Mindyak massifs are composed mainly of lherzolites with subordinate harzburgites and dunites, while harzburgites predominate in the Kempirsai massif and dunites with large chromitite deposits are significantly developed in its southeastern part. The PT–fO_2 formation conditions of lherzolites correspond to the upper mantle below a rift structure: temperature of 700–1000 °C, pressure of 5–12 kbar, and oxygen fugacity varying from –2 to + 0.5 ΔFMQ. The compositional variations of Cr-spinels from primitive lherzolite (Cr# 0.15–0.30, Mg#0.6–0.8) to harzburgite (Cr# 0.3–0.6, Mg#0.5–0.7) and dunite (Cr# 0.6–0.8, Mg#0.4–0.7) and the increase in Mg# value of olivine are a result of synchronous processes of partial melting and plastic flow of the material in the upper mantle. Four main morphological Cr-spinel types are distinguished in lherzolites: (1) fine rods and lamellae within silicate grains and along their boundaries, (2) anhedral and holly-leaf grains closely intergrown with restitic olivine and enstatite, (3) anhedral and subhedral grains in an assemblage with plagioclase and diopside and (4) euhedral grains in dunites. The formation of type 1 grains is interpreted as a result of deformation-induced segregation of trace elements on structural defects of silicates with consequent crystallization of newly formed minerals. The advanced stages of solid-phase transformation produce the larger anhedral and holly-leaf grains in peridotites and euhedral grains in dunites (types 2 and 4 grains). The decompression replacement of a precursor high-pressure mineral (garnet?) is suggested for the formation of the Cr-spinel–plagioclase aggregates. The subhedral and euhedral grains in the assemblage with plagioclase and clinopyroxene could have formed as a result of crystallization from percolating melts or their reaction with restite.

Keywords Chromian spinel · Lherzolite · Dunite · EBSD · South Urals · Ophiolites

Introduction

It is well known that Cr-spinel is a sensitive indicator of the formation conditions of mantle rocks (e.g., Dick and Bullen 1984; Kamenetsky et al. 2001) and, in particular, ultramafic rocks of the mantle section of ophiolite complexes (e.g., Arai 1994). Their compositions are used for the estimation of the degree of partial melting of mantle (Arai 1980; Morishita et al. 2006) or the interpretation of geodynamic settings of various igneous complexes (Arai 1994; Barnes and Roeder 2001) and metamorphic transformations of rocks during their ascending into the upper crust.

The morphological features of Cr-spinels are no less important. The morphology of accessory Cr-spinel and its relation to the textural features of host peridotites and rock-forming silicates in mantle ophiolitic ultramafic rocks and

Editorial handling: J. Elsen

✉ Dmitry E. Saveliev
savl71@mail.ru

[1] Institute of Geology, Ufa Federal Research Centre, Russian Academy of Sciences, 16/2 Karl Marx St., 450077 Ufa, Russian Federation

[2] Geomodel Resource Center, St. Petersburg State University, St. Petersburg 198504, Russia

[3] Abylkas Saginov Karaganda Technical University, Karaganda 100027, Kazakhstan

[4] Institute of Geology, Ufa Federal Research Centre RAS, Ufa 450077, Russian Federation

xenoliths have been studied in details in the 1970s–1980s before the application of quantitative methods of microstructural analysis became common (Mercier and Nicolas 1975; Nielson-Pike and Schwarzman 1977; Leblanc 1980).

As was shown in early studies of ophiolites and mantle xenoliths, there is a link between the morphology of Cr-spinels and structural features of mantle rocks (Mercier and Nicolas 1975; Nielson-Pike and Schwarzman 1977). In mantle section of ophiolites, the morphological characteristics of Cr-spinels regularly vary depending on the composition and structural–textural features of host rock (Leblanc 1980; Johnson 2012): lherzolites (the less depleted rocks of the mantle section) typically contain anhedral (vermicular) Cr-spinel; the increase in #Cr values (in harzburgites) is associated with the formation of cuspate (subhedral) Cr-spinel and, in dunites, the accessory Cr-spinel regularly exhibits an euhedral habit.

In the early period of studies of Cr-spinel, the deformation structures of host ultramafic rocks were classified and the changes in the morphology of Cr-spinels were considered to be mostly related to the processes of partial melting, recrystallization and annealing (e.g., Mercier and Nicolas 1975). At the same time, the origin of euhedral Cr-spinel in dunites of the transitional mantle–crust zone was interpreted, as a rule, as a result of cumulative process (e.g., Leblanc 1980; Noller and Carter 1986). According to some authors, the difference in morphology of Cr-spinel in various rocks is related to the results of prevalence of either of partial melting (anhedral) or cumulative precipitation (euhedral) (Noller and Carter 1986; Matsumoto and Arai 2001).

The presence of inclusions of olivine and other silicates in Cr-spinel is a key factor, according to which the dunites were considered cumulative (Auge 1987), although Nielson-Pike and Schwarzman (1977) cautioned against this simplified interpretation indicating that the metamorphic rocks also host poikiloblasts, which formed as a result solid-state processes.

Later, along with development of a dominant melt–rock interaction model (Kelemen 1990; Zhou et al. 1994; Arai and Yurimoto 1994), the formation of dunite-hosted Cr-spinel was considered to be a result of interaction of peridotites with percolating boninitic or basaltic melts (Zhou et al. 1994; Leblanc 1995; Rollinson 2005). This idea was often based on their improbable crystallization due to simple differentiation (e.g., Tamura et al. 2016). Arai and Yurimoto (1994) suggested that the melt, which formed at a depth with higher pressure, percolates inside the mantle harzburgites and reacts with them dissolving orthopyroxene and forming dunite and secondary SiO_2- and Cr-rich melt. The latter mixes with further portion of relatively primitive melt and deposits Cr-spinel. Numerous studies favor these interpretations, however, a comprehensive microstructural analysis of these rock associations seems to be lacking.

Studies of mineral inclusions in both accessory and ore Cr-spinel from ophiolites (Auge 1987; McElduff and Stumpfl 1991; Miura et al. 2012; Borisova et al. 2012; Johan et al. 2017) showed that the composition only of few inclusions corresponds to those of minerals from host rocks (e.g., Moutte 1982). In most cases, the composition of inclusions significantly differs from the compositions of possible parental or mantle-interacted melts (e.g. Johan et al. 2017). These inclusions are called exotic (Johan et al. 2017) and considered a result of multiple reaction of mantle ultramafic rocks with percolating melts of various compositions (e.g., Arai and Miura 2016) or fluids (Borisova et al. 2012; Johan et al. 2017). These morphological and compositional features of Cr-spinel are still unclear within an accepted melt/rock interaction concept (e.g., Kelemen et al. 1995) or mixing of melts (e.g., Ballhaus 1998).

In our alternative model, the compositional and morphological diversity of accessory Cr-spinels in ophiolitic peridotites is resulted from two related processes: partial melting of the mantle substrate and simultaneous/subsequent solid-state transformation including plastic flow (deformation), recrystallization and annealing. The detailed study of fine Cr-spinel rods in silicates is especially important for recognition of solid-state processes in the upper mantle peridotites. In this work, we applied the microstructural electron back-scattered diffraction (EBSD) to reveal the morphological and chemical diversity of chromites in Uralian ultramafic massifs and suggest a model of chromite formation.

In previous work (Saveliev et al. 2021), we have investigated in detail a formation mechanism of tiny Cr-spinel precipitations in rock-forming silicates on the example a few fresh lherzolite samples from the Kraka massif and shown that the initial fine Cr-spinels in the form of rods or lamellae were formed on defects in the structure of the host silicate minerals (olivine and orthopyroxene) by segregation of impurities or by heterogeneous nucleation in the zones of greatest crystalline lattice distortion (zones of predominant recrystallisation). In this paper, we are making a wider review of morphological and compositional features of accessory Cr-spinels in four most representative ophiolite ultramafic massifs of the South Urals in order to classify them and study in more detail the formation mechanisms of each type.

Brief geological background

The Uralian fold belt consists of several longitudinal zones, which replace each other from the eastern margin of the East European Platform to the Mesozoic sedimentary cover of the West Siberian Platform, which overlaps the eastern part of the fold belt. According to Puchkov (1997), the Urals includes the following lithotectonic zones: Uralian Foredeep, West

Uralian Zone, Central Uralian Zone, Main Uralian Fault Zone, Tagil–Magnitogorsk Zone and East Uralian Zone (Fig. 1a). The first three zones represent an ancient passive continental margin of the East European Platform and are separated from the paleoisland-arc complexes of the Tagil–Magnitogorsk Zone by the Main Uralian Fault Zone. The ophiolitic ultramafic rocks with an area of ~ 10 000 km^2 are abundant in the southern part of the fold belt (Fig. 1b), mostly in the Main Uralian Fault Zone, Sakmara paleobasin and marginal parts of the Magnitogorsk Megazone as well as the East Uralian Uplift. The ultramafic bodies form several parallel longitudinal belts: Western (1), Main Uralian Fault (2), Miass–Kulikovsky (3), Kazbaevo (4), and Eastern (5) (Fig. 1b).

The longest belt of the Main Uralian Fault divides the paleocontinental and paleooceanic sectors of the paleo-Uralian basin. Small ultramafic bodies also occur in the Uraltau, Ufaley, and Ilmeny–Vishnevogorsk metamorphic complexes. Most ultramafic bodies are small, longitudinally elongated and include completely serpentinized and tectonized rocks. The intensity of their metamorphic transformations increases from the west to the east. The Western belt is dominated by low-temperature mesh serpentinites, the central belts also contain antigorite serpentinites, and the massifs of the Kazbaevo belt are totaly composed of antigorite serpentinites and talc–carbonate rocks. The ultramafic rocks of the Eastern belt underwent mostly mesh serpentinization.

The largest massifs are Kraka (belt 1), Ufaley, Talovsky, Nurali, Mindyak, Khabarny, Khalilovo, Kempirsai (belt 2), Tatishchevo, Varshavka (belt 4), and Akkarga (belt 5) (Fig. 1). The relatively wide areas of relict peridotites occur only in the massifs of the belts 1, 2 and 5 whereas the other massifs are completely serpentinized.

According to the classification of (Nicolas et al. 1971; Boudier and Nicolas 1985), the ultramafic rocks (non-serpentinized protoliths) of the South Urals were subdivided into lherzolite and harzburgite types on the basis of petrographic and geochemical features (Savelieva 1987; Saveliev et al. 2008). The harzburgite massifs are most abundant and include the largest Kempirsai massif, which is famous for the unique chromite deposits with total reserves of > 300 Mt (Pavlov et al. 1968). The lherzolite massifs tend to concentrate in the western flank of the fold belt. The most representative massifs are Kraka, Nurali, and Mindyak (Figs. S1 and S2). The freshest rocks in the Kraka massif are exposed in the Northern and Central blocks.

Analytical methods

The peridotite samples with minimum mesh serpentinization were collected during field works, which were conducted at the Kraka, Nurali, Mindyak and Kempirsai ultramafic massifs in 2000–2021. The petrographic study of samples was conducted using optical microscopy in transmitted and reflected polarized light.

The bulk chemical composition of 23 peridotite samples was analyzed in the Chemical Laboratory of the Institute of Geology, Ufa Federal Research Center, Russian Academy of Sciences (IG UFRC RAS, Ufa, Russia). The SiO_2, Al_2O_3, TiO_2, and P_2O_5 contents were determined by photometry, Na_2O and K_2O contents were measured in flame photometer, the $FeO + Fe_2O_3$ content was analyzed by volumetric method, CaO and MgO contents were determined by titration and losses on ignition (LOI) were measured by weight method. The compositions of rocks are given in Table S1, and normative mineralogical compositions are given in Fig. S3.

The composition of rock-forming silicates and accessory Cr-spinels was determined on a Tescan Vega 3 SBH and Tescan Vega 4 Compact SEM equipped with an Oxford Instruments Energy Dispersive X-Ray EDS at the Institute for Metals Superplasticity Problems and Institute of Geology of Ufa Federal Research Centre, Russian Academy of Sciences (Ufa, Russia). The spectra were automatically processed using the AzTec One software package employing the TrueQ technique. The electron beam accelerating voltage was 20 kV with a current of 4 nA and a beam size of 3 µm. X-ray acquisition time was 60 s in spot-mode.

The elemental compositions were quantified using standard samples of natural and synthetic compounds. The formulas of chromian spinels were calculated for three cations. The proportion of ferrous and ferric iron in the formula of chromian spinels was determined by the stoichiometry of the mineral. The atomic ratios in spinel ($Cr\# = Cr/(Cr + Al)$ and $Mg\# = Mg/(Mg + Fe^{2+})$), olivine ($Fo = Mg/(Mg + Fe)$) and pyroxenes ($En = Mg/(Mg + Fe + Ca)$; $Di = Ca/(Mg + Fe + Ca)$; $Fs = Fe/(Mg + Fe + Ca)$) were calculated on the basis of the chemical analysis. The $\Delta\log(fO_2)$ value was calculated using the formula from (Ballhaus et al. 1991).

The details of the internal structure of four rock samples (enstatite K0852), lherzolite K1992 and N0258 and dunite N0260) were studied with EBSD on a Hitachi S-3400 N SEM equipped with an Oxford NordlysNano EBSD detector at the GEOMODEL Resource Centre (St. Petersburg State University, St. Petersburg) at a 30-kV accelerating voltage, a 5-nA beam current and a beam focused to a point not exceeding 100 nm in diameter. All samples were cut subperpendicular to foliation, impregnated in epoxy resin and polished. In the final preparation stage, argon ion polishing was performed (Oxford IonFab 300, a 10-min exposure, a 500-V accelerating voltage, a 200-mA beam current, Nanophotonics Resource Centre, St. Petersburg State University) to remove a mechanically deformed layer from the surface.

The EBSD patterns were recorded in the form of reflection of an incident electron beam from a 70º pre-tilted sample on a luminescent screen. The fact that a diffraction event

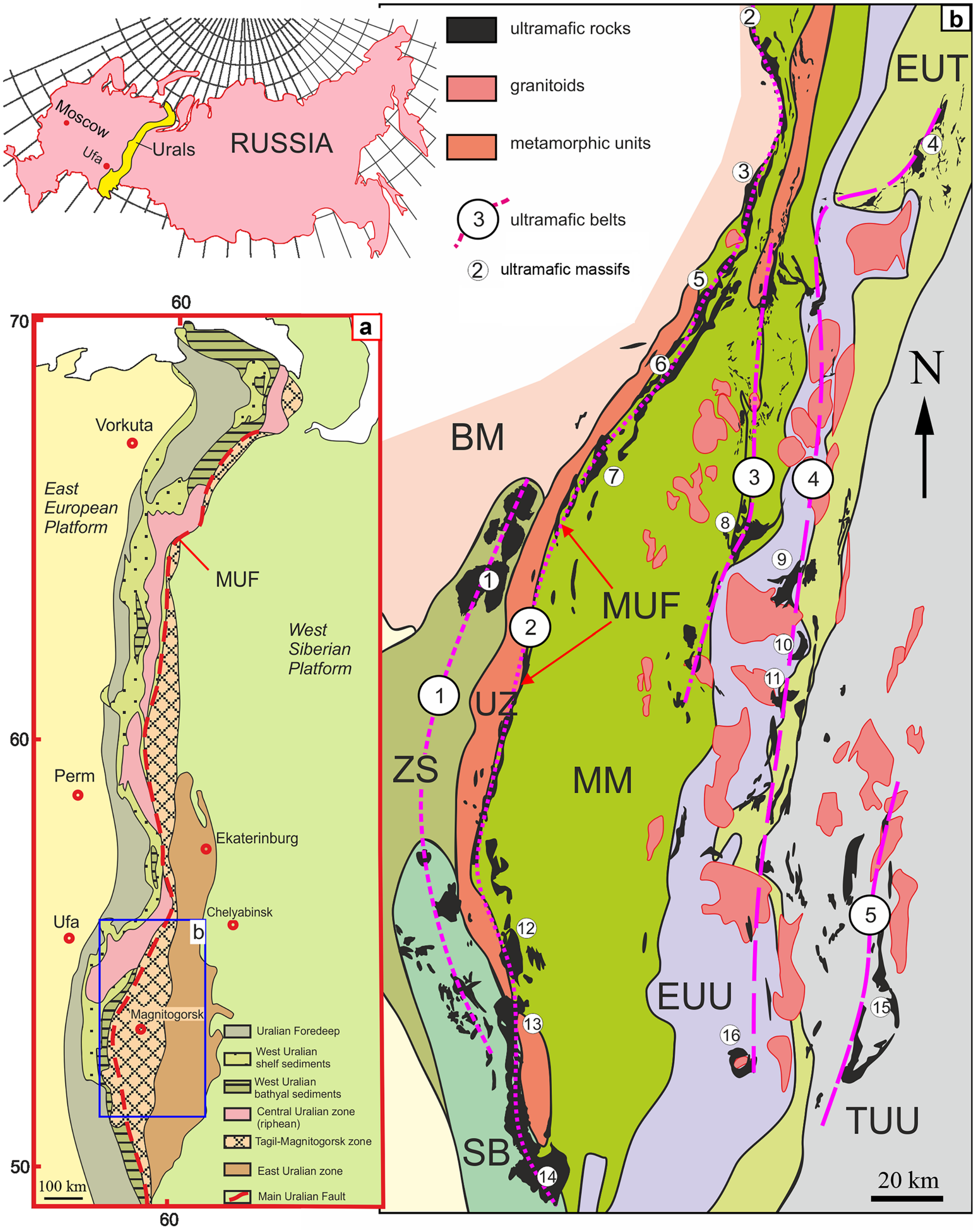
Moscow
Ufa
Urals
RUSSIA
ultramafic rocks
granitoids
metamorphic units
3 ultramafic belts
2 ultramafic massifs
a
70
60
50
60
60
Vorkuta
East European Platform
MUF
West Siberian Platform
Perm
Ekaterinburg
Ufa
Chelyabinsk
b
Magnitogorsk
Uralian Foredeep
West Uralian shelf sediments
West Uralian bathyal sediments
Central Uralian zone (riphean)
Tagil-Magnitogorsk zone
East Uralian zone
Main Uralian Fault
100 km
b
EUT
BM
MUF
UZ
ZS
MM
EUU
SB
TUU
N
20 km
1
2
3
4
5
6
7
8
9
10
11
12
13
14
15
16

◂**Fig. 1** **a** Schematic geological map of the Uralian fold belt, after Puchkov (1997); **b** Distribution of ophiolitic ultramafic rocks in the South Urals**.** Ultramafic belts: 1, Western (Kraka–Mednogorsk); 2, Main Uralian Fault Zone; 3, Miass–Kulikovsky; 4 Kazbaevo; 5, Eastern. Ultramafic massifs: 1, Kraka; 2, Ufaley; 3, Talovsky; 4, Muslyumovo; 5, Nurali; 6, Kalkan; 7, Mindyak; 8, Kulikovsky; 9, Tatishchevo; 10, Verbl'yuzh'egorsky; 11, Varshavka; 12, Khalilovo; 13, Khabarny; 14, Kempirsai; 15, Akkarga; 16, Kiembay. Colors highlight different structural zones: ZS, Zilair Synclinorium; SB, Sakmara basin; UZ, Uraltau Zone; MM, Magnitogorsk Megazone; EUU, East Uralian Uplift; EUT, East Uralian Trough; TUU, Trans Uralian Uplift

is spatially limited by beam size on the surface and several tens of nanometres in depth makes EBSD a efficient high resolution method for microstructural characterization.

Due to high quality of diffraction patterns and high symmetry of the studied phases, 4 × 4 binning was performed during data acquisition, allowing the acquisition frequency to be raised to 30–50 Hz. In order to filter misinterpretations, averaging of two frames was applied. Acquired patterns were automatically indexed using Oxford AztecHKL software with predefined phases (olivine ICSD 9334; orthopyroxene ICSD 37313; chromite ICSD 20819) in a Hough space with a resolution of 100. All matching solutions are characterised by an error value of mean angle deviation (MAD) from theoretical diffraction pattern and a number of matching bands. The MAD values rarely exceed 0.6° what is considered a good match. Following the procedure, all the solutions were placed on the map according to an inverse pole figure (IPF) colour scheme, where the colour coordinate corresponds to a specific orientation. The maps were refined using an algorithm for removing standalone solutions that have no neighbours; solutions were also added to non-indexed points having 9 or 8 neighbours belonging to the same grain of the same phase. No further data filtering was applied.

Microstructural and microtextural mapping of Cr-spinel, olivine and orthopyroxene grains was performed. All the EBSD orientation maps are coloured according to IPF colour scheme based on the orientation of the grains. Red, green and blue colours are attributed to Cr-spinel grains, which < 100 > , < 110 > , and < 111 > axes, respectively, are perpendicular to Z direction, comprising the normal to the sample surface.

Results

Petrography of ultramafic rocks

The ultramafic rocks studied are fully crystalline rocks, which are replaced by mesh serpentine, the content of which varies from few to 100 vol. % up to the complete replacement

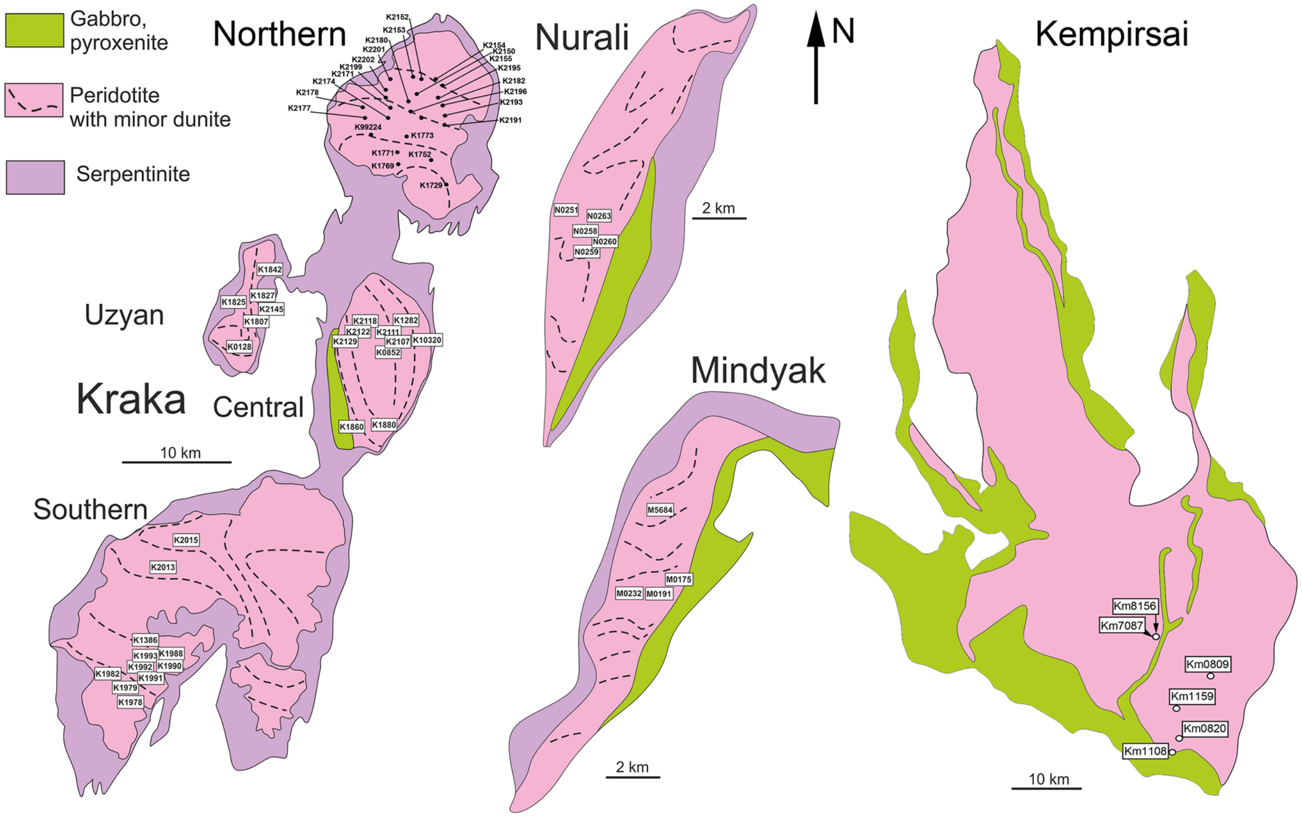

Fig. 2 Schematic geological maps of the Kraka, Nurali and Mindyak lherzolite massifs

with pseudomorphs of olivine and pyroxenes. The location of the studied samples is shown on the geological sketch maps (Fig. 2). Below, we describe the freshest samples of ultramafic rocks.

Olivine and orthorhombic pyroxene are the main rock-forming silicates in ultramafic rocks. In thin sections, they exhibit the features of high-temperature plastic deformation in form of undulatory extinction (Fig. 3a–e), which is caused by bending of the crystal due to the presence of dislocations (Passchier and Trouw 2005), subgrains in olivine (Fig. 3a, b), kink-bands, bending orthopyroxene grains and plane structural elements (cleavage fractures) (Fig. 3d, f).

Deformed enstatite contains numerous lamellae of Ca-pyroxene or amphibole inside the grain (Fig. 3d–g) that are irregularly distributed. In addition to thin lamellae, orthopyroxene often hosts isometric inclusions of diopside and/or pargasite and, in this case, the areas 30–50 µm wide around these grains are lamellae-free (Fig. 3d, g). The formation of these lamellae is probably related to coalescence of several parallel lamellae (Saveliev and

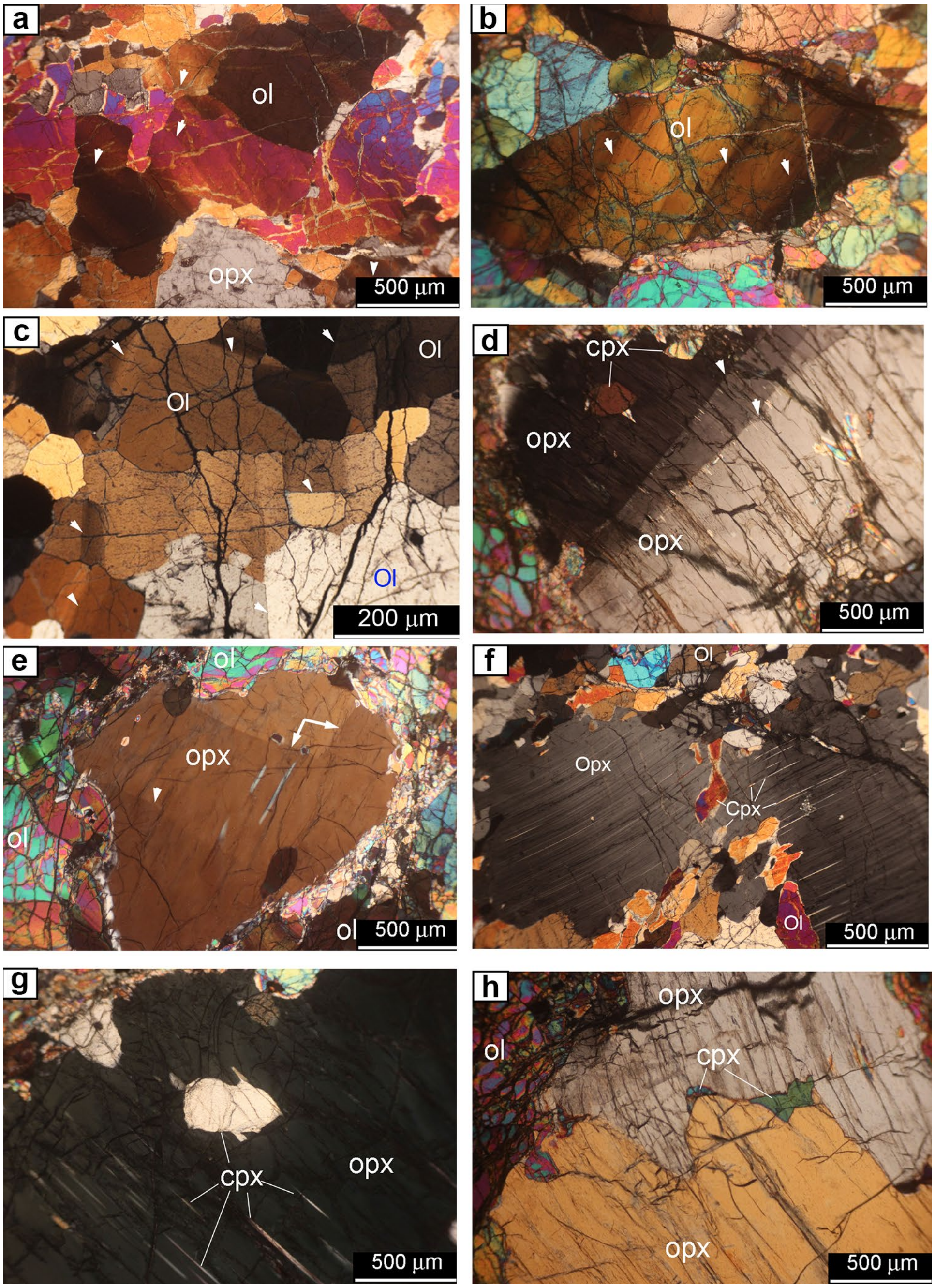

Fig. 3 Petrographic features of lherzolites from Uralian ophiolitic complexes: **a–c** deformed olivine grains (**a**, **b** sample K2150, **c** sample Km7087), **d–f** deformed and folded enstatite grains with lamellae and neoblasts of diopside, enstatite II and olivine (**d** sample K2152, **e** sample K2150, **f** sample Km7087), **g** diopside inclusion (neoblast) in deformed enstatite grain and its lamellae (sample K2150), **h** newly formed fine diopside grains at the boundary between large recrystallized enstatite grains (sample K2150). White arrows show low-angle grain boundaries. Here and below: K – Kraka, N – Nurali, M – Mindyak, Km – Kempirsai

Musabirov 2019), which is evident from local preservation relict branches oriented according to lamellar structure inside the host mineral (Fig. 3g).

Plastic deformation of olivine and orthopyroxene is accompanied by syntectonic recrystallization, which promotes the formation of porphyroclastic structure with large deformed grains (1–4 mm in size) and aggregates of smaller subisometric neoblasts (commonly 10–200 μm in size) along their periphery (Fig. 3e). The lower degree of the deformation of orthopyroxene can lead to annealing, which typically follows by the formation of optically homogeneous grains and transformation of low-angle (subgrain) boundaries into high-angle boundaries (Fig. 3h) commonly with smaller diopside and olivine grains, which primary formed as deformation-induced inclusions (Saveliev et al. 2017, 2021).

Monoclinic Ca-pyroxene (diopside), amphibole (pargasite), plagioclase and Cr-spinel are less abundant minerals of ultramafic rocks. Diopside occurs either as small grains in lherzolites or as deformation-induced inclusions in enstatite in both lherzolites and harzburgites. Pargasite is found only as inclusions in plastically deformed enstatite in lherzolites and harzburgites. Cr-spinel is an ordinary accessory mineral of ultramafic rocks and characterized by widely variable morphological and compositional features (as described below).

The presence of plagioclase in ultramafic rocks allows us to distinguish the spinel–plagioclase lherzolites, which are subordinate in the Southern and Uzyan blocks of the Kraka massif, more abundant in its Northern and Central blocks and are comparable in distribution to plagioclase-free lherzolites in the Nurali and Mindyak massifs. In most samples, plagioclase was found in intergrowths with Cr-spinel and rarely as individual anhedral grains.

Morphology of Cr-spinel

Macroscopic grains

In ultramafic rocks, Cr-spinel exhibits diverse morphology: from skeletal and vermicular grains in lherzolites to euhedral crystals in dunites as well documented in many ophiolite massifs worldwide (Leblanc 1980; Johnson 2012; Matsumoto and Arai 2001). Thus, below, we emphasize only some genetically important features, which have not been sufficiently characterized in previous works.

In ultramafic massifs of the South Urals, the accessory Cr-spinel in dunites, harzburgites and poorly disseminated chromitites demonstrate mostly euhedral morphology (Fig. 4a, b). Cr-spinel exhibits rounded boundaries, rare branches directed toward the silicate matrix and single or numerous inclusions of silicates, which include both matrix (olivine, orthopyroxene) and “exotic” (diopside, pargasite, phlogopite, etc.) minerals (e.g., Johan et al. 2017). Fine Cr-spinel inclusions could occur in silicates in form of rods (olivine) or lamellae (orthopyroxene). The Cr-spinel also forms chains of the grains in dunites and chromitites (Fig. 4b).

Lherzolites contain abundant anhedral and rare subhedral Cr-spinel. In comparison with Cr-spinels from dunites and harzburgites, those from lherzolites are typically characterized by branches (Fig. 4c–f), which were termed holly leaf texture (Nielson-Pike and Schwarzman 1977; Johnson 2012) or fish hooks (Yudovskaya et al. 2019). Numerous vermicular Cr-spinel grains are most commonly associated with plagioclase and typically occupy the central parts of the Cr-spinel–plagioclase aggregates.

In holly-leaf grains, the branches penetrate into the silicate matrix typically separating fragments of plastically deformed crystals of olivine, orthopyroxene or diopside. The next stage of the growth of these branches may result in a full enclosure of the silicate fragments that become mineral inclusions inside the Cr-spinel grain (Fig. 5) with the sizes of trapped silicate inclusions being comparable with the sizes of host mineral (Fig. 5a–c, f). In other cases, the silicate-hosted Cr-spinel grains occur inside larger silicate minerals of the same composition (Fig. 5e–h).

Tiny grains

Numerous tiny Cr-spinel grains (0.1–10 μm in size) occur in silicate minerals (olivine, enstatite, diopside) and along their boundaries in addition to relatively large grains (50–2000 μm) (Fig. 6a–d). In plastically deformed olivine grains, Cr-spinel forms elongated rods up to 70 μm long and less than 1 μm wide (Fig. 6a) and, commonly, occurs along structural defects (boundaries of kink-bands and dislocation tilt walls). The Cr-spinel rods are unevenly distributed in thin sections. The smallest pargasite inclusions (0.5–10 μm in size) in olivine and enstatite grains are observed close to Cr-spinel.

In addition to lamellae of silicate minerals, the plastically deformed pyroxene grains commonly contain platy Cr-spinel inclusions 10–30 μm in length (Fig. 6b). The finest Cr-spinel grains are also often observed along the boundaries between plastically deformed olivine and pyroxenes (Fig. 6c) or in a recrystallization area amid small subisometric equigranular neoblasts of enstatite (Opx_2), diopside, forsterite and pargasite (Fig. 6d). The finer Cr-spinel grains are commonly confined to their larger counterparts at the boundaries of silicates (Fig. 6e). In some places, the complex morphology of chromite aggregates indicates that coalescence of finer Cr-spinel grains is responsible for the formation of larger Cr-spinel crystals with composite silicate inclusions (e.g., Fig. 6f).

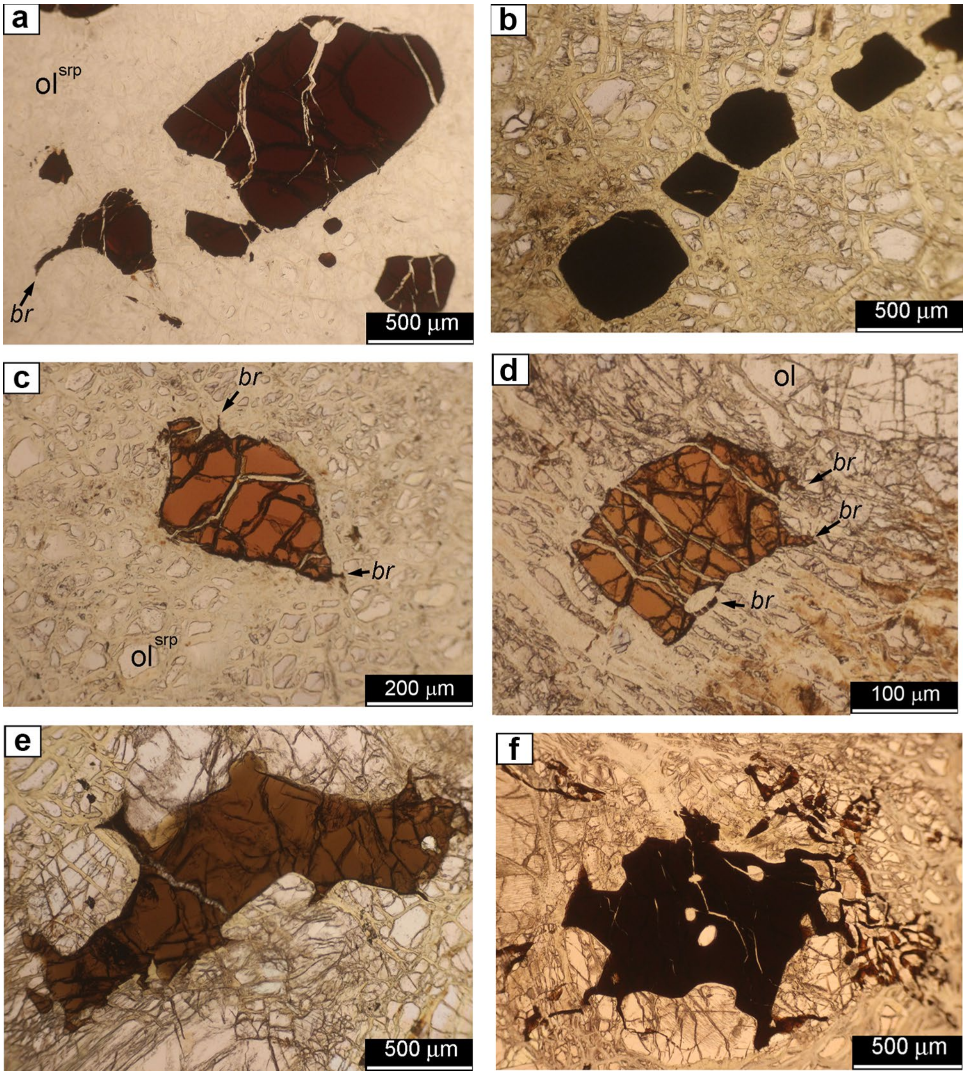

Fig. 4 Morphological diversity of Cr-spinel in harzburgite, dunite and lherzolite from Uralian ophiolitic complexes: **a** large smoothly rounded subhedral Cr-spinel grain with Ol inclusion and serpentine veinlets and smaller branched (br) Cr-spinel grains in serpentinized olivine (sample K2150), **b** chains of euhedral Cr-spinel grains in dunite (sample K2171), **c** subhedral branched Cr-spinel grains in strongly serpentinized olivine (sample K2202), **d – f** anhedral to vermicular Cr-spinel grains with elongated branches into olivine (**d** sample K2202, **e** sample K2174, **f** sample Km0809). Photos **a – f** polarized transmitted light

Spinel-plagioclase assemblages

The lherzolites of the mantle section of the Kraka, Nurali, and Mindyak massifs often contain specific mineral assemblages of Cr-spinels and plagioclase. These minerals typically form intimate intergrowths and their proportion in rock can reach 10–15 vol. %. In case of their elevated proportion, they form seams or bands, which mark primary banding and foliation of peridotites.

In most cases, plagioclase is intensely altered up to saussurite and prehnite and rarely albite. In freshest lherzolites of the Nurali massif, the Cr-spinel–plagioclase aggregates are characterized by sharp boundaries with matrix, which is mostly composed of olivine and orthopyroxene (Fig. 7). The aggregates are either isometric (Fig. 7a, b) or flattened (Fig. 7c, d). The Cr-spinel always occurs in the central part of the aggregates and exhibits a skeletal morphology, plagioclase typically occurs in peripheral parts of the aggregates (Fig. 7a–c). In elongated aggregates, the marked order is often disturbed by deformation and the skeletal shape of the spinel is less pronounced. (Fig. 7c, d).

Individual separate grains of Cr-spinel and plagioclase are rare that is typical of several lherzolite samples of the Mindyak massif, where Cr-spinel occurs as small subhedral and euhedral crystals whereas saussuritized plagioclase forms isometric and anhedral grains 150–250 µm in size or numerous grains up to their network in assemblage with diopside, enstatite and olivine (Fig. 7e, f).

Chemical composition of Cr-spinel and associated silicates

The composition of accessory Cr-spinel from the studied massifs varies widely (Table 1) that is typical of the ophiolitic complexes. Cr-spinel is associated with high-Mg olivine ($Fo_{89–95}$) (Fig. 8a). In triangle diagram, the compositions of Cr-spinel are located close to the Al–Cr side indicating an isomorphic substitution of these elements (Fig. 8b).

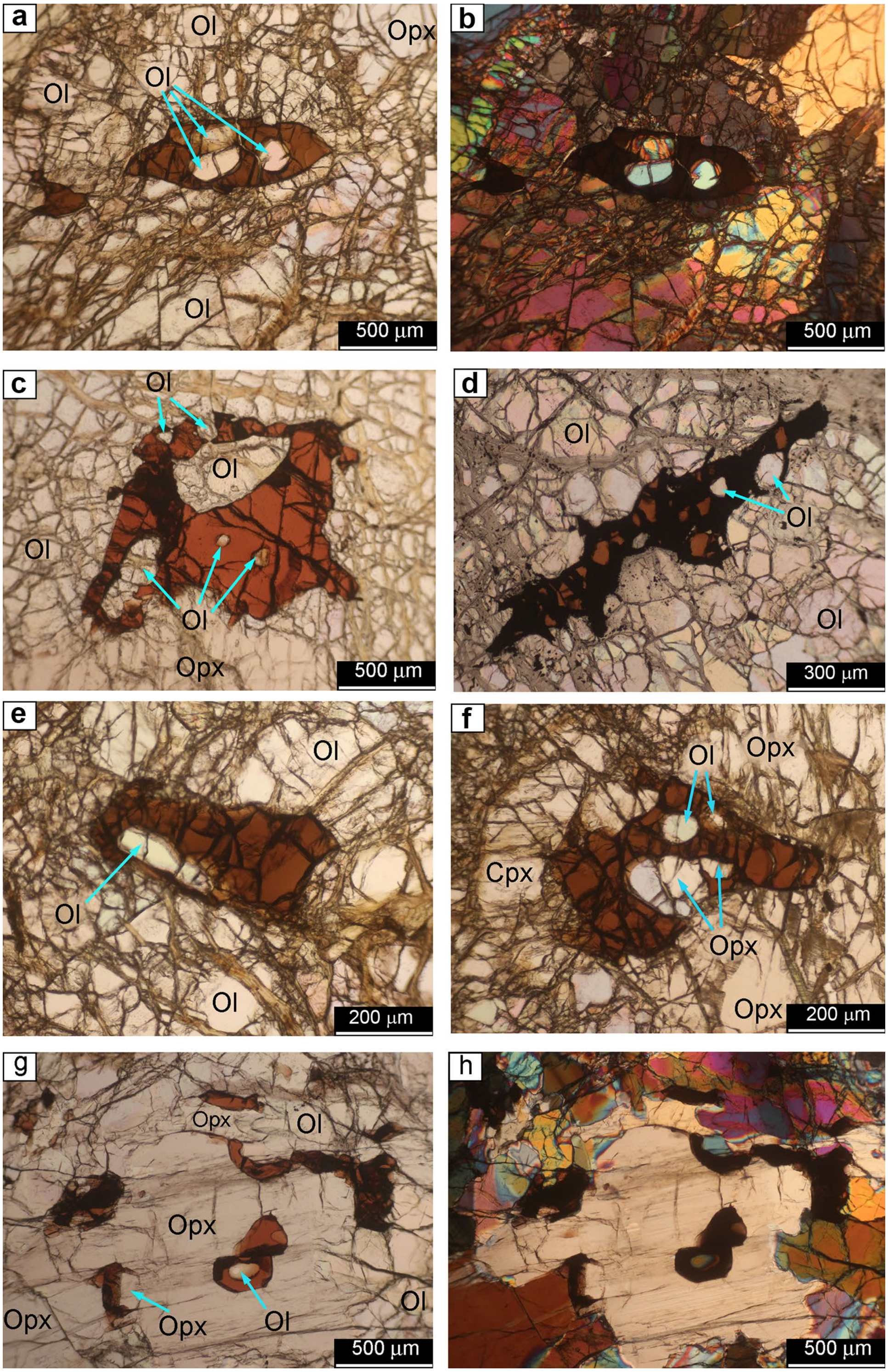

Fig. 5 Cr-spinel with silicate inclusions in lherzolite from Kraka massifs: **a – f** anhedral to vermicular branched inclusion-rich Cr-spinel grains in olivine (**a–b**, **e–f** sample K2193, **c** sample K2182, **d** sample K2150), **g** and **h** Cr-spinel grains of various morphological types associated with large orthopyroxene (Opx) grain and Cr-spinel grains with small olivine and enstatite inclusions (sample K2199). Photos **a**, **c – g** polarized transmitted light, **b**, **h** cross-polarized transmitted light

The FeO + Fe_2O_3 content of accessory Cr-spinel increases from lherzolites to dunites and its Cr# values (Cr/(Cr + Al) at.%) positively and negatively correlates with Fe_2O_3 content and Mg# values (Mg/(Mg + Fe^{2+}) at.%), respectively (Fig. 8c). In contrast, the Cr-spinel from the massive ore seams and ore bands exhibits another trend (Fig. 8c): the constantly high Cr# values (0.7–0.8) are accompanied by significantly variable Mg# values, which generally increase from dunite toward ore.

Less abundant pyroxenes in rocks include orthopyroxene (enstatite) and clinopyroxene (diopside), which are characterized by relatively constant compositions

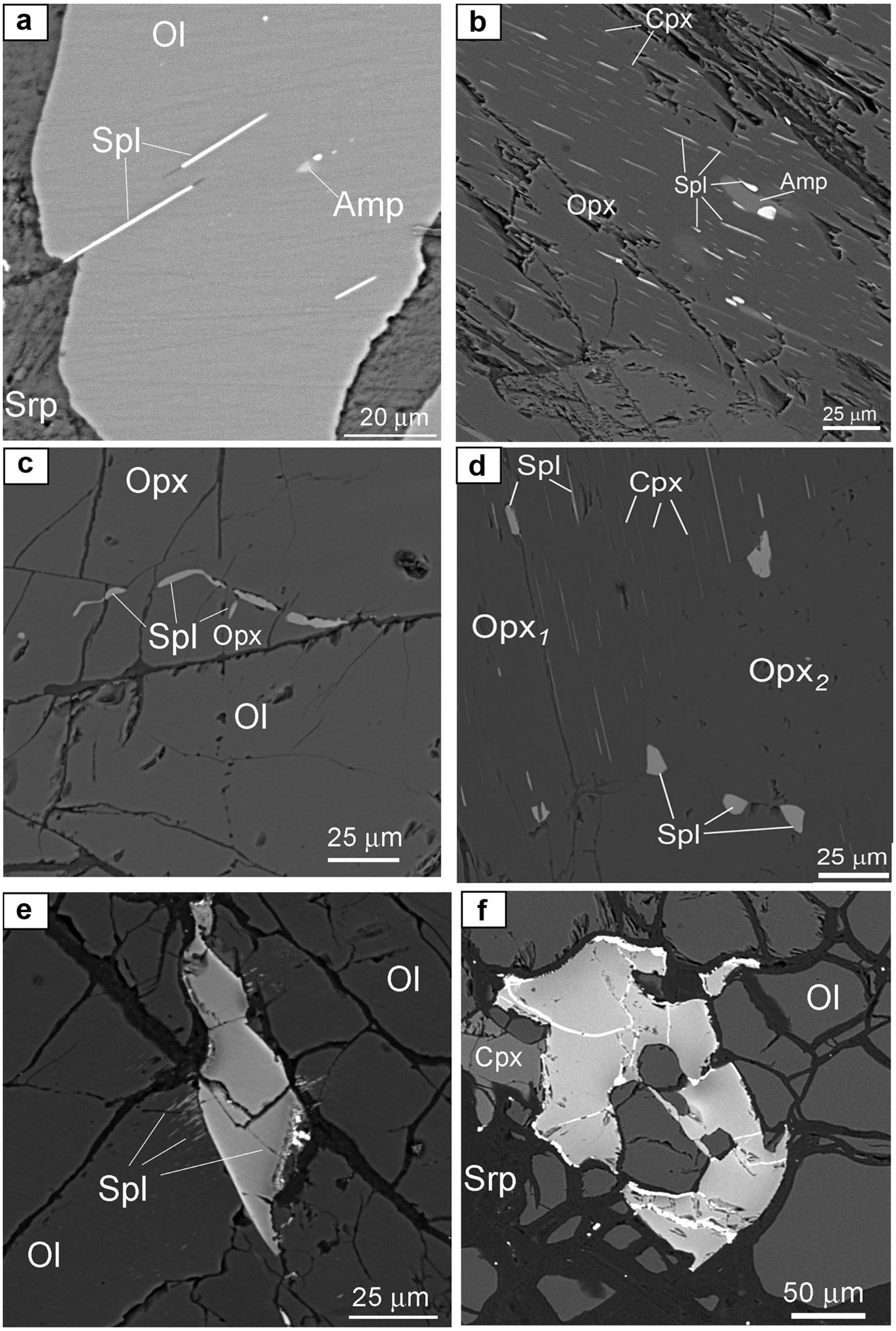

Fig. 6 BSE-images of tiny, branched and holly leaf spinel grains from harzburgite and lherzolite from Uralian ophiolitic complexes: **a** tiny Cr-spinel (Spl) rods in olivine with amphibole inclusions (sample N0260), **b** numerous lamellae of Cr-spinel and diopside as well as amphibole grains in deformed Opx porphyroclast (sample Km0820), **c** chain of elongated Cr-spinel grains at the boundary between orthopyroxene porphyroclast and neoblast (sample K2178), **d** fine Cr-spinel grains in recrystallization zone between larger deformed orthopyroxene porphyroclasts (sample Km0820), **e** anhedral Cr-spinel at the olivine grain boundary and numerous parallel Cr-spinel rods in olivine (sample K99224), **f** anhedral branched Cr-spinel grain with silicate inclusions (sample K1729)

(Tables 2 and 3). The amount of ferrosilite end-member component varies within 7.40–9.75 and 2.30–4.64 mol.% in enstatite and diopside, respectively. Both monoclinic and orthorhombic pyroxenes are characterized by significantly variable contents of trace elements (Cr and Al).

The Al_2O_3 content of enstatite varies from 0.4 to 5.4 wt %: the highest contents are typical of large porphyroclasts from lherzolites, whereas the lowest Al_2O_3 contents are detected in enstatite grains from harzburgites with low amount of pyroxenes and in enstatite neoblasts from lherzolites. Chromium behaves similarly: the highest Cr_2O_3 contents (0.60–0.77 wt %) correlate with high Al_2O_3 contents in large grains from lherzolites and the lowest contents (< 0.3 wt %) are determined in neoblasts and rare enstatite grains in harzburgites.

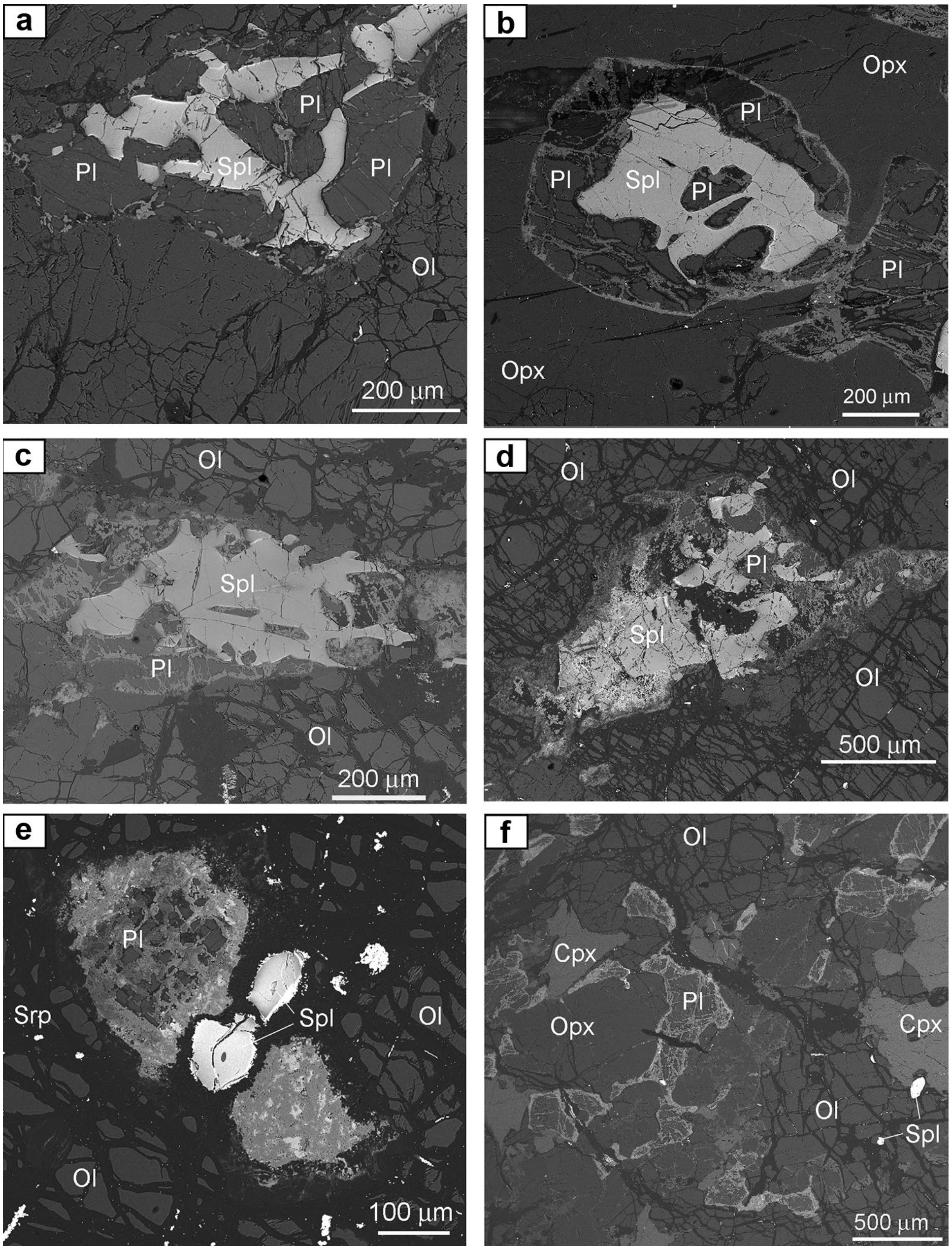

Fig. 7 Spinel–plagioclase aggregates in lherzolites from Uralian ophiolitic complexes: **a** skeletal Cr-spinel in the central part of plagioclase (Pl) aggregate (sample K1771); **b** equigranular Cr-spinel–plagioclase aggregate surrounded by large orthopyroxene grains (sample N258); **c** and **d** flattened Cr-spinel–plagioclase aggregate composed of anhedral Cr-spinel in a core and a plagioclase rim, as well as plagioclase inclusions in Cr-spinel (**c** – sample K2176, **d** – sample K99224); **e** assemblage of equigranular saussurised plagioclase and zoned subhedral spinel grains (sample M5684); **f** anhedral plagioclase grains between olivine, enstatite and diopside grains (sample M0191)

In diopside, the variations in the Al_2O_3 contents are comparable with those of enstatite (1.50–6.45 wt % in large grains) whereas Al_2O_3 contents of some neoblasts, which occur close to the deformed porphyroclasts of enstatite, decreases below the microprobe detection limit. The Cr_2O_3 content of monoclinic pyroxene is higher than that of orthorhombic pyroxene and ranges from 0.30 to 1.52 wt %.

Formation conditions of ultramafic rocks

The formation temperatures of ultramafic rocks were estimated using two-pyroxene and Cr-spinel–olivine geothermometers (Wells 1977; Wood and Banno 1973; Brey and Köhler 1990; Ballhaus et al. 1991; Roeder et al. 1979; Fabries 1979; Ono 1983). The oxygen fugacity (fO_2) was determined using oxybarometer (Ballhaus et al. 1991) and the FeO and Fe_2O_3 contents are calculated according to the stoichiometry of minerals.

In Cr#–fO_2 diagram, the compositions of studied samples significantly vary and their majority corresponds to a range of –1.5 to 1 relatively to a FMQ buffer (Fig. 8d), which is generally consistent with data on other ultramafic massifs of the Urals (Chashchukhin and Votyakov 2009) and worldwide (Ballhaus et al. 1991).

Table 1 Selected analyses of chromian spinel grains from massifs of South Urals

##	1	2	3	4	5	6	7	8	9	10	11	12	13	14	15	16	17	18
#sample	K1729	K1752	K1769	K1771	K1773	K2152	K2153	K2177	K2178	K2180	K2184	K2191	K2195	K2196	K10320	K1282	K1860	K1880h
rock	LZ-HB	LZ-HB	LZ-HB	LZ	LZ-HB	LZ	LZ	LZ	LZ	HB	D-HB	LZ	LZ	LZ-HB	LZ	LZ	D-MTZ	D-HB
Spl type	2	2	2	2	2	2	2	2	2	2	4	2	2	2	2	2	4	4
TiO_2	–	–	–	–	–	0.22	–	–	–	–	0.28	–	–	–	–	–	0.25	–
Al_2O_3	41.44	44.48	37.63	41.14	44.88	33.51	51.96	37.83	44.52	34.93	14.83	51.17	42.38	40.47	43.75	43.03	13.05	22.77
FeO	14.56	12.42	15.62	18.19	12.95	18.09	12.35	21.82	17.62	16.58	24.66	13.68	14.94	20.62	15.32	14.71	18.95	18.79
MnO	–	–	–	–	–	–	–	–	–	–	–	–	–	–	–	–	–	0.58
MgO	16.50	18.08	15.38	16.22	17.97	14.68	19.57	14.48	16.32	14.58	8.95	18.78	17.07	14.54	15.88	16.62	13.73	12.81
Cr_2O_3	26.42	23.87	30.41	23.79	23.08	32.50	15.32	25.24	20.84	33.64	50.74	17.95	25.61	23.90	24.17	26.23	54.41	45.36
NiO	–	–	–	–	–	–	–	–	–	–	–	–	–	–	–	–	–	–
V_2O_3	0.25	–	–	0.22	–	0.28	–	–	–	–	0.26	–	–	–	–	–	–	0.40
ZnO	–	–	–	–	–	–	–	–	–	–	–	–	–	0.47	–	–	–	–
Sum	99.18	98.85	99.05	99.56	98.87	99.28	99.20	99.38	100.0	99.74	99.73	101.6	100.0	100.0	99.13	100.8	100.9	100.7
#Cr	0.30	0.26	0.35	0.28	0.26	0.39	0.17	0.31	0.24	0.39	0.70	0.19	0.29	0.28	0.27	0.29	0.74	0.57
#Mg	0.69	0.75	0.66	0.67	0.74	0.64	0.78	0.62	0.68	0.63	0.43	0.74	0.70	0.62	0.67	0.68	0.65	0.59
Fo-Ol	0.924	0.914	0.914	0.904	0.911	0.910	0.913	0.907	0.907	0.923	0.914	0.910	0.918	0.878	0.910	0.902	0.939	0.918

##	19	20	21	22	23	24	25	26	27	28	29	30	31	32	33	34	35	36
#sample	K1880d	K1880h	K2107	K2111	K2118	K2122	K2145	K0128	K1807	K1825	K1827	K1842	K1386	K1978	K1979	K1982	K1991	K1992
rock	D	HB	HB	LZ	LZ	HB	D	LZ	LZ-HB	LZ-HB	LZ-HB	LZ-HB	LZ	LZ-HB	D	LZ-HB	D	LZ-HB
Spl type	4	4	2	2	2	2	4	2	2	2	2	2	2	2	4	2	4	2
TiO_2	0.26	–	–	–	–	–	–	–	–	0.22	–	0.36	–	–	0.17	–	–	–
Al_2O_3	15.85	28.20	9.26	39.21	30.49	19.23	12.05	54.63	31.84	36.54	40.20	30.23	44.35	39.39	9.71	49.93	27.55	40.29
FeO	22.40	19.08	27.20	16.38	19.73	20.41	19.17	12.64	16.97	16.07	14.59	16.77	15.39	16.04	21.91	12.64	18.25	16.01
MnO	0.36	0.05	0.00	0.00	0.00	0.00	–	–	–	–	–	–	–	–	–	0.31	0.56	–
MgO	10.63	13.28	7.12	16.13	14.17	12.02	12.17	19.27	14.70	15.29	16.65	14.94	17.05	15.69	9.69	17.51	13.43	15.43
Cr_2O_3	50.26	38.71	56.01	27.78	36.38	49.17	56.17	14.05	36.50	31.88	28.29	37.43	22.61	28.25	59.48	18.86	40.71	27.44
NiO	–	–	–	–	–	–	–	–	–	–	–	–	–	–	–	0.26	–	–
V_2O_3	0.32	0.29	–	–	–	–	–	–	–	–	0.27	0.27	0.25	0.27	–	–	–	–
ZnO	–	–	–	0.32	–	–	–	–	–	–	–	–	–	–	–	–	–	–
Sum	100.1	99.61	99.58	99.83	100.8	100.9	99.55	100.58	100.00	100.00	100.00	100.00	99.65	99.65	100.96	99.52	100.49	99.17
#Cr	0.68	0.48	0.80	0.32	0.44	0.63	0.76	0.15	0.43	0.37	0.32	0.45	0.25	0.32	0.80	0.20	0.50	0.31
#Mg	0.51	0.60	0.37	0.69	0.63	0.56	0.59	0.76	0.64	0.64	0.70	0.66	0.70	0.67	0.48	0.71	0.60	0.65
Fo-Ol	0.921	0.916	0.909	0.908	0.914	0.917	0.931	0.900	0.920	0.915	0.925	0.927	0.899	0.913	0.942	0.914	0.912	0.915

Table 1 (continued)

##	37	38	39	40	41	42	43	44	45	46	47	48	49	50	51	52	53	54
#sample	K1993	K2013	K2015	K2015	M5684	M0175	M0232	N0251	N0258	N0259	N0260	N0263	Km0820	Km0820	Km1108	Km1108	Km1108	Km1108
rock	LZ	HB	HB	D	LZ	LZ	LZ	LZ	LZ-HB	LZ-HB	D	LZ-HB	LZ-HB	LZ-HB	LZ-HB	LZ-HB	LZ-HB	LZ-HB
Spl type	2	2	4	4	3	3	3	2	3	2	4	2	2	1	2	1	2	2
TiO_2	–	–	–	0.28	0.34	–	0.37	–	–	–	0.26	–	–	–	–	–	–	–
Al_2O_3	51.11	28.48	29.70	14.40	34.55	39.88	29.81	43.70	32.92	21.95	13.89	27.43	22.81	31.16	28.32	30.03	46.08	43.66
FeO	13.15	16.73	16.68	16.19	19.41	18.02	23.07	17.60	18.04	24.12	22.47	23.25	24.26	20.38	18.62	17.81	15.34	16.14
MnO	0.24	–	–	–	–	–	–	–	–	–	–	–	–	–	–	–	–	–
MgO	17.80	13.21	13.07	13.97	13.87	15.75	11.80	15.47	14.77	10.28	11.17	12.33	11.48	13.37	13.67	13.85	16.88	16.22
Cr_2O_3	17.00	40.69	39.36	54.68	31.83	26.35	33.59	23.01	35.05	42.50	52.21	37.21	39.43	32.86	38.51	37.34	21.85	24.31
NiO	–	–	–	–	–	–	–	–	–	–	–	–	–	–	–	–	–	–
V_2O_3	–	–	0.24	–	–	–	0.29	0.23	–	0.26	–	–	0.26	–	–	0.25	0.25	0.21
ZnO	–	–	0.24	–	–	–	–	0.39	–	–	–	–	–	0.44	–	–	–	–
Sum	99.31	99.11	99.29	99.51	100.00	100.00	98.93	100.00	102.87	99.11	100.00	100.22	98.25	98.19	99.11	99.28	100.40	100.52
#Cr	0.18	0.49	0.47	0.72	0.38	0.31	0.43	0.26	0.42	0.56	0.72	0.48	0.54	0.41	0.48	0.45	0.24	0.27
#Mg	0.71	0.60	0.58	0.66	0.61	0.67	0.54	0.65	0.64	0.48	0.54	0.55	0.53	0.60	0.62	0.62	0.70	0.67
Fo-Ol	0.903	0.926	0.915	0.920	0.904	0.928	0.893	0.913	0.921	0.900	0.923	0.911	0.92	0.92	0.92	0.93	0.92	0.92

##	55	56	57	58	59	60	61	62	63	64	65	66	67	68
#sample	Km8156	Km8156	Km8156	Km8156	Km7087	Km7087	Km7087	Km7087	Km1159	Km1159	Km1159	Km0809	Km0809	Km0809
rock	LZ-HB	LZ-HB	LZ-HB	LZ-HB	LZ-HB	LZ-HB	LZ-HB	LZ-HB	LZ-HB	LZ-HB	LZ-HB	LZ-HB	LZ-HB	LZ-HB
Spl type	2	2	4	2	4	2	2	4	2	2	1	2	2	2
TiO_2	–	–	–	–	–	–	–	–	–	–	–	–	–	–
Al_2O_3	43.05	30.05	29.05	41.90	33.85	46.06	47.03	31.20	39.87	36.23	42.57	33.48	34.45	33.71
FeO	15.05	18.22	17.83	14.54	17.01	12.98	13.72	16.61	14.37	14.36	12.16	17.59	17.34	19.04
MnO	–	–	–	–	–	–	–	–	–	–	–	–	–	–
MgO	16.16	13.95	14.20	16.24	14.88	17.52	17.62	14.84	15.50	15.23	17.35	14.62	14.10	13.47
Cr_2O_3	24.94	37.53	38.91	26.91	34.25	23.21	21.62	37.08	28.12	32.14	26.92	32.83	32.11	31.32
NiO	–	–	–	–	–	–	–	–	–	–	–	–	–	–
V_2O_3	0.30	0.25	–	–	–	0.22	–	0.27	–	–	–	0.22	–	–
ZnO	0.51	–	–	0.39	–	–	–	–	–	–	–	–	–	0.39
Sum	100.00	100.00	100.00	100.00	100.00	100.00	100.00	100.00	97.86	97.96	99.01	98.73	98.01	97.93
#Cr	0.28	0.46	0.47	0.30	0.40	0.25	0.24	0.44	0.32	0.37	0.30	0.40	0.38	0.38
#Mg	0.67	0.61	0.63	0.67	0.64	0.72	0.72	0.65	0.66	0.66	0.72	0.63	0.63	0.60
Fo-Ol	0.93	0.93	0.93	0.93	0.93	0.93	0.93	0.93	0.93	0.92	0.92	0.93	0.92	0.92

Here and below, a dash means an element concentration less than limit of detection; FeO = FeO+Fe_2O_3; Fo-Ol is Mg/(Mg + Fe), at.% in adjacent olivine grain; Spl type corresponds to that in the text

The calculation of temperatures of mineral equilibria according to various geothermometers yields subsolidus values in all cases (Fig. 8e, f). The orthopyroxene–clinopyroxene and olivine–Cr-spinel pairs of the same samples, however, exhibit distinct temperatures (higher by 200 °C on average according to the two-pyroxene thermometer). Similar differences are typical of both ophiolite and oceanic peridotites (e.g., Bazylev 2003) that is explained by a different rate of diffusion of various elements in mineral pairs used (e.g., Ozawa 1983). A range of the calculated temperatures for olivine–Cr-spinel equilibrium in our samples is 550–990 °C in contrast to a 750–1200 °C range according to two-pyroxene geothermometer. Pressure was estimated using two-pyroxene geobarometer (Putirka 2008). In the Kraka, Nurali and Mindyak massifs, it varies from 5 to 12 kbar (Fig. S4) that corresponds to the transition between spinel- and plagioclase-facies in mantle peridotites (Green and Falloon 1998). Along with the similar values, in the Kempirsai massif, values up to 17 kbar were obtained.

Microstructure of Cr-spinel and host silicates according to EBSD

Lherzolite from the Central Kraka massif (sample K0852) is composed of large crystals (up to 30 mm) of deformed enstatite with numerous inclusions of diopside, pargasite and Cr-spinel (Fig. 9). It was recently shown using optical methods that the lamellae of diopside and Cr-spinel in this sample occur along planes (100) of the host mineral, probably, as a result of plastic deformation of enstatite (Saveliev and Musabirov 2019; Saveliev et al. 2021). Pargasite is confined to low-angle boundaries between enstatite domains and rarely occurs as small inclusions in enstatite.

The EBSD studies confirmed a domain structure of both enstatite (Fig. 9a, b) and large holly leaf Cr-spinel grains, which occur at the boundary junction of the enstatite domains (Fig. 9a, d). The branches of these grains are parallel to lamellae (Fig. 9a) and the internal parts are divided

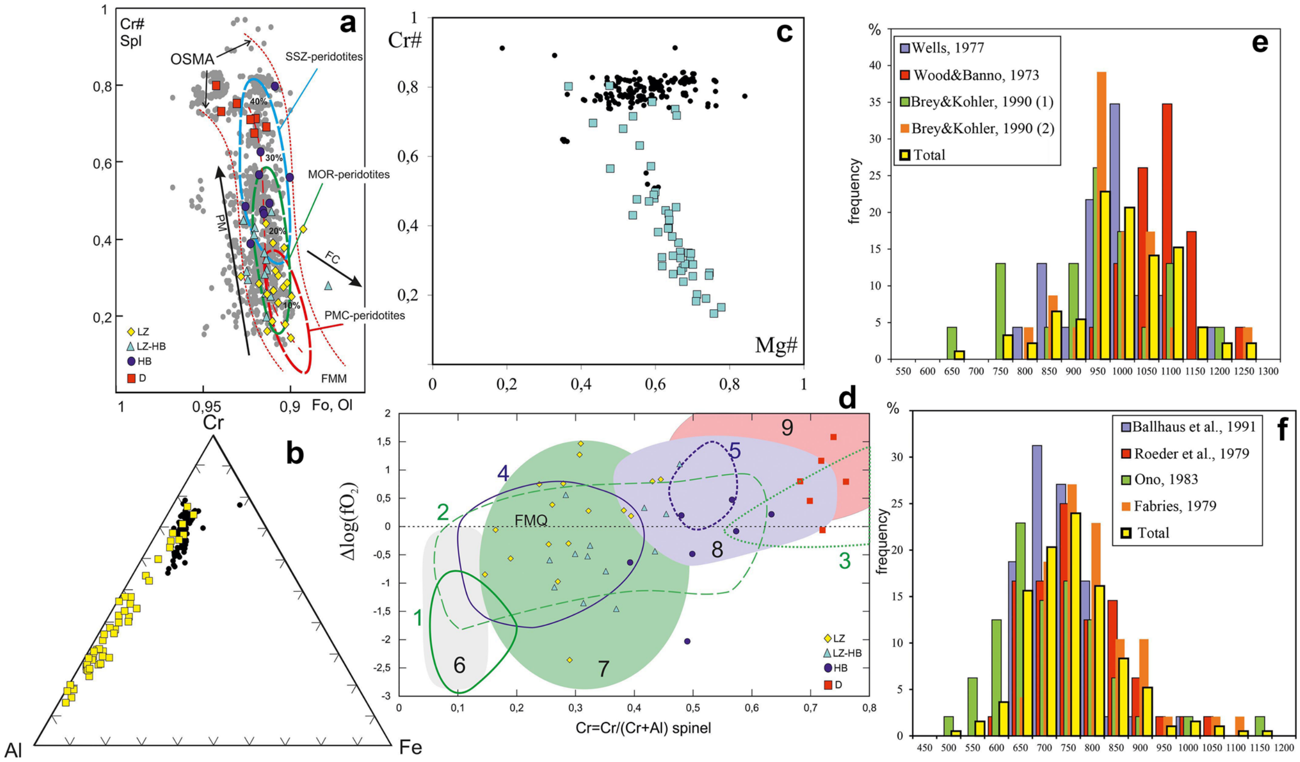

Fig. 8 Compositional features of Cr-spinel and silicates from from Uralian ophiolitic complexes: **a** compositions of associated olivine and Cr-spinel grains from peridotites after (Arai 1994) ("OSMA diagram" – olivine-spinel mantle association), trends and fields are after (Jaques and Green 1980; Arai 1994), gray markers are single analyses from peridotites of various massifs of the South Urals, after (Saveliev 2018, 2019); **b** and **c** compositions of Cr-spinel from South Urals peridotites (yellow markers) on Al–Cr–Fe (**b**) and Cr#–Mg# (**c**) diagrams; black markers, compositions of ore-forming Cr-spinel grains from the same massifs, after (Saveliev 2018), **d** correlation between fO_2 and Cr# value of accessory Cr-spinel from South Urals peridotites (countered fields, after (Ballhaus et al. 1991): 1–3, peridotite xenoliths: 1, primitive; 2, slightly metasomatized; 3, strongly metasomatized; 4, 5, abyssal peridotites with spinel (4) and plagioclase (5); colored fields, after (Ahmed et al. 2016; Arai and Ishimaru 2008; Parkinson and Pearce 1998): 6 – primitive mantle, 7 – abyssal peridotites, 8 – fore-arc peridotites, 9 – oceanic arc peridotites); **e** and **f** distribution of mineral-equilibrium temperatures in South Urals peridotites according to various geothermometers: **e** – two-pyroxene (Wells 1977; Wood and Banno 1973; Brey and Köhler 1990 (1)) and one-Opx (Brey and Kohler 1990 (2)), **f** – olivine-spinel (Ballhaus et al. 1991; Roeder et al. 1979; Fabries 1979; Ono 1983); LZ – lherzolite, HB – harzburgite, D – dunite

Table 2 Selected analyses of enstatite grains from massifs of South Urals

##	1	2	3	4	5	6	7	8	9	10	11	12	13	14	15	16	17	18
#sample	K1752	K1769	K1771	K1773	K2177	K2178	K2180	K2184	K2191	K2195	K10320	K1282	K1880	K1880	K2107	K2118	K0128	K1807
rock	LZ-HB	LZ-HB	LZ	LZ-HB	LZ	LZ	HB	D-HB	LZ	LZ	LZ	LZ	D-HB	HB	HB	LZ	LZ	LZ-HB
SiO_2	54.47	55.24	54.62	54.56	52.84	54.06	55.84	55.89	54.19	54.86	53.96	55.69	57.32	56.59	57.45	56.61	56.25	56.31
TiO_2	–	–	–	–	–	–	0.22	–	–	–	–	–	–	–	–	–	–	–
Al_2O_3	3.83	3.00	2.80	3.32	5.38	3.63	2.27	0.87	3.97	3.38	5.19	4.68	1.52	1.45	0.40	3.14	2.30	1.02
FeO	5.78	6.04	6.23	6.01	6.24	6.47	5.10	5.94	6.09	5.62	5.46	6.18	5.78	5.54	6.12	6.35	6.72	5.31
MnO	–	–	–	–	–	–	–	–	–	–	–	–	–	–	–	–	0.23	–
MgO	34.15	34.35	34.20	34.08	33.18	33.53	35.63	35.18	33.65	34.35	33.07	34.17	34.15	35.40	35.98	35.07	34.75	35.70
CaO	0.59	0.74	0.66	0.62	0.70	0.87	0.57	0.67	1.02	0.69	1.22	0.53	0.82	0.47	0.71	0.64	0.28	0.32
Cr_2O_3	0.77	0.76	0.44	0.57	0.66	0.61	0.72	0.38	0.64	0.72	0.73	0.61	0.41	0.54	0.32	0.66	0.32	0.00
Sum	99.60	100.14	98.94	99.16	99.01	99.18	100.35	98.93	99.57	99.61	99.62	101.86	100.00	100.00	100.99	102.47	100.9	98.67
Formula coefficients																		
Si	1.879	1.898	1.898	1.891	1.836	1.878	1.906	1.938	1.874	1.891	1.864	1.883	1.976	1.941	1.953	1.902	1.921	1.950
Ti	–	–	–	–	–	–	0.006	–	–	–	–	–	–	–	–	–	–	–
Al-IV	0.121	0.102	0.102	0.109	0.164	0.122	0.094	0.062	0.126	0.109	0.136	0.117	0.024	0.059	0.047	0.098	0.079	0.050
Al-VI	0.035	0.020	0.012	0.027	0.056	0.027	0.000	0.000	0.035	0.029	0.075	0.069	0.038	0.000	0.000	0.026	0.014	0.000
Fe	0.166	0.173	0.181	0.174	0.181	0.188	0.145	0.172	0.176	0.162	0.157	0.174	0.166	0.159	0.174	0.178	0.192	0.153
Mn	–	–	–	–	–	–	–	–	–	–	–	–	–	–	–	–	0.007	–
Mg	1.756	1.759	1.771	1.761	1.718	1.736	1.812	1.819	1.734	1.765	1.702	1.721	1.755	1.810	1.823	1.756	1.769	1.843
Ca	0.022	0.027	0.025	0.023	0.026	0.032	0.021	0.025	0.038	0.025	0.045	0.019	0.030	0.017	0.026	0.023	0.010	0.012
Cr	0.021	0.021	0.012	0.016	0.018	0.017	0.019	0.010	0.018	0.020	0.020	0.016	0.011	0.015	0.009	0.017	0.009	0.000
##	**19**	**20**	**21**	**22**	**23**	**24**	**25**	**26**	**27**	**28**	**29**	**30**	**31**	**32**	**33**	**34**	**35**	
#sample	K1825	K1842	K1386	K1978	K1982	K1992	K1993	M0232	M5684	N0251	N0258	N0259	N0263	Km0820	Km0820	Km1108	Km1108	
rock	LZ-HB	LZ-HB	LZ	LZ-HB	LZ-HB	LZ-HB	LZ	LZ	LZ	LZ	LZ	LZ-HB	LZ-HB	LZ-HB	LZ-HB	LZ-HB	LZ-HB	
SiO_2	55.97	56.96	53.61	56.11	56.40	57.04	56.29	54.91	53.40	55.48	56.42	55.54	55.24	56.27	55.91	55.41	56.40	
TiO_2	–	–	–	–	–	–	–	0.24	0.20	–	–	–	–	–	–	–	–	
Al_2O_3	1.49	1.02	4.44	3.17	2.52	3.14	3.24	2.45	3.97	1.95	2.74	1.27	2.04	1.28	1.35	2.04	1.75	
FeO	5.97	5.18	6.38	5.61	5.66	5.93	6.05	6.71	6.41	5.94	6.49	6.70	5.99	5.71	5.79	5.80	5.54	
MnO	–	–	–	–	0.16	–	–	–	–	–	–	0.27	–	–	0.22	–	–	
MgO	35.10	36.21	33.27	33.44	32.54	33.46	32.93	34.11	33.40	34.98	34.48	34.78	34.60	35.72	35.50	34.85	35.33	
CaO	0.48	0.37	0.63	0.58	1.92	0.53	0.83	0.93	0.62	0.67	1.01	0.59	0.94	0.24	0.25	0.52	0.48	
Cr_2O_3	0.34	0.27	0.64	0.67	0.25	0.74	0.40	0.64	0.57	0.20	0.61	0.45	0.61	0.22	0.34	0.50	0.39	
Sum	99.34	100.0	98.97	99.58	99.44	100.8	99.75	100.0	98.56	99.23	101.8	99.61	99.42	99.43	99.35	99.12	99.90	

Table 2 (continued)

##	19	20	21	22	23	24	25	26	27	28	29	30	31	32	33	34	35
Formula coefficients																	
Si	1.934	1.947	1.866	1.943	1.962	1.955	1.951	1.895	1.866	1.917	1.912	1.921	1.910	1.948	1.941	1.929	1.943
Ti	–	–	–	–	–	–	–	0.006	0.005	–	–	–	–	–	–	–	–
Al-IV	0.066	0.053	0.134	0.057	0.038	0.045	0.049	0.105	0.134	0.083	0.088	0.079	0.090	0.052	0.059	0.071	0.057
Al-VI	0.000	0.000	0.048	0.072	0.065	0.082	0.083	0.000	0.030	0.000	0.022	0.000	0.000	–	–	0.013	0.014
Fe	0.172	0.148	0.185	0.162	0.164	0.170	0.175	0.193	0.187	0.171	0.183	0.193	0.173	0.165	0.168	0.168	0.159
Mn	–	–	–	–	0.005	–	–	–	–	–	–	0.008	–	–	0.007	–	–
Mg	1.807	1.844	1.726	1.726	1.687	1.709	1.701	1.754	1.740	1.802	1.742	1.792	1.783	1.843	1.837	1.809	1.815
Ca	0.018	0.014	0.024	0.022	0.072	0.019	0.031	0.034	0.023	0.025	0.037	0.022	0.035	0.009	0.009	0.019	0.018
Cr	0.009	0.007	0.018	0.018	0.007	0.020	0.011	0.018	0.016	0.006	0.016	0.012	0.017	0.006	0.009	0.014	0.011

by low-angle boundaries with significant misorientation near the branches (up to 5°) in contrast to the central parts of the grains (Fig. 9d). The euhedral grains and grains with smoothed contours are characterized by a homogeneous internal structure.

Similarly to the above example, the anhedral Cr-spinel grains around olivine in lherzolite from the Southern Kraka massif (sample K1992) exhibit a step-like domain structure, whereas subhedral and euhedral grains are homogeneous (Fig. S5a, c). The Fig. S4b shows the separation of a primary large orthopyroxene porphyroclast into two parts with a misorientation value between them of 15–20° and the formation of a wedged recrystallization zone (RZ). This zone is characterized by the presence of neoblasts of enstatite, diopside and olivine, as well as newly-formed euhedral homogenous Cr-spinel grains (Fig. S5b, d).

The microstructure of skeletal Cr-spinel grains is considered on an example of lherzolite of the Nurali massif (Fig. 10). Here, the Cr-spinel is associated with high-temperature silicates (olivine and enstatite), which both surround Cr-spinel and occur as inclusions (Fig. 10b, grains 1–6) of various morphology: euhedral (grain 5), subhedral (grains 3, 6), and anhedral (grains 2, 4).

The Cr-spinel, which overgrows silicates, is characterized by a heterogeneous structure, the domains of which are divided by low-angle boundaries and show a misorientation angle of up to 10° (Fig. 10c, e, f, profiles 1–2) similarly to the above cases. At the same time, the outlines of Cr-spinel are close to euhedral with evident five apices and three connecting edges. The domain boundaries are generally characterized by gradual transitions (Fig. 10e, f) with small steps up to 5–6°.

Almost all olivine and orthopyroxene grains, which are completely or partially enclosed in Cr-spinel grains, are also composed of differently oriented domains, which are divided by low-angle boundaries (Fig. 10c, d, g, f, profiles 3–4) except for two small grains 2 and 4. The misorientation character (straight sharp boundaries) inside grains 3, 5 and 6 most likely indicates that the domain boundaries formed as a result of translation sliding (i.e., plastic deformation), which is most evident in olivine 5 with a sharp peak in misorientation angle reaching 18° (Fig. 10g).

Olivine in ultramafic rocks commonly contains Cr-spinel rods, which were found in lherzolites, harzburgites, and dunites of the Kraka, Nurali and Kempirsai massifs. The decoration of the dislocation structure of dunite sample N0260 showed that the Cr-spinel rods are regularly confined to dislocation tilt walls (Fig. 11). At the same time, the areas with similar rods studied with EBSD showed a homogeneous structure of host olivine where the misorientation angle does not exceed the resolution of the method.

Table 3 Selected analyses of diopside grains from massifs of South Urals

##	1	2	3	4	5	6	7	8	9	10	11	12	13	14	15	16	17
#sample	K1752	K1769	K2153	K2177	K2180	K2191	K2195	K1282	K1860	K1880	K2111	K2118	K0128	K1807	K1825	K1827	K1842
rock	LZ-HB	LZ-HB	LZ	LZ	HB	LZ	LZ	LZ	D-MTZ	D-HB	LZ	LZ	LZ	LZ-HB	LZ-HB	LZ-HB	LZ-HB
SiO_2	52.94	52.87	51.78	51.23	52.89	51.28	53.28	53.21	54.34	53.50	52.54	53.87	52.63	55.11	54.18	53.53	53.83
TiO_2	–	–	0.36	–	–	–	–	0.50	–	–	–	–	–	–	–	–	0.32
Al_2O_3	3.95	3.02	6.12	6.45	3.85	5.33	3.99	5.29	0.68	1.85	3.46	1.72	4.17	–	1.14	1.93	1.80
FeO	1.79	2.04	2.21	2.76	2.33	2.33	2.29	2.44	2.39	1.91	2.35	2.12	2.35	1.53	1.93	1.80	1.50
MgO	17.03	17.72	15.72	15.72	18.85	16.12	17.26	17.03	17.47	17.13	17.52	18.25	16.98	18.79	18.87	18.20	17.72
CaO	22.60	23.40	21.52	22.19	20.24	22.46	21.96	21.50	24.88	24.15	23.36	23.93	23.31	24.31	23.64	23.89	23.83
Na_2O	0.69	–	1.07	0.56	–	–	–	0.59	–	0.20	–	–	–	–	–	–	–
Cr_2O_3	1.01	0.96	1.22	1.08	1.33	1.14	1.23	0.95	0.51	0.92	0.77	0.44	0.83	0.26	0.24	0.66	1.00
Sum	100.00	100.00	100.00	100.00	99.50	98.65	100.00	101.52	100.27	99.66	100.00	100.32	100.28	100.00	100.00	100.00	100.00
Formula coefficients																	
Si	1.911	1.916	1.872	1.858	1.919	1.890	1.935	1.897	1.972	1.949	1.904	1.944	1.906	1.992	1.956	1.937	1.954
Ti	–	–	0.010	–	–	–	–	0.013	–	–	–	–	–	–	–	–	0.009
Al-IV	0.089	0.084	0.128	0.142	0.081	0.110	0.065	0.103	0.028	0.051	0.096	0.056	0.094	0.008	0.044	0.063	0.046
Al-VI	0.079	0.045	0.132	0.133	0.084	0.122	0.106	0.119	0.001	0.028	0.052	0.017	0.084	–	0.005	0.019	0.031
Fe	0.054	0.062	0.067	0.083	0.071	0.072	0.070	0.073	0.072	0.058	0.071	0.064	0.071	0.046	0.058	0.054	0.045
Mg	0.916	0.957	0.847	0.850	1.019	0.885	0.934	0.905	0.944	0.930	0.946	0.981	0.916	1.012	1.015	0.981	0.958
Ca	0.875	0.909	0.834	0.863	0.788	0.888	0.855	0.822	0.968	0.943	0.908	0.926	0.905	0.942	0.915	0.927	0.928
Na	0.048	–	0.075	0.039	–	–	–	0.041	–	0.014	–	–	–	–	–	–	–
Cr	0.029	0.027	0.035	0.031	0.038	0.033	0.035	0.027	0.015	0.026	0.022	0.013	0.024	0.007	0.007	0.019	0.029

##	18	19	20	21	22	23	24	25	26	27	28	29	30	31	32	33
#sample	K1386	K1978	K1982	K1992	K1993	M0175	M0232	M5684	N0251	N0259	N0260	N0263	Km0820	Km0820	Km1108	Km1108
rock	LZ	LZ-HB	LZ-HB	LZ-HB	LZ	LZ	LZ	LZ	LZ	LZ-HB	D	LZ-HB	LZ-HB	LZ-HB	LZ-HB	LZ-HB
SiO_2	50.70	52.51	53.76	53.85	55.06	54.28	51.41	52.52	52.08	53.70	51.71	53.36	51.49	53.96	53.72	54.00
TiO_2	0.52	–	0.15	–	–	–	0.63	0.41	0.55	–	–	–	–	–	–	–
Al_2O_3	4.76	3.62	2.44	2.21	1.32	2.13	4.08	2.70	4.48	2.14	4.72	3.17	6.71	0.74	1.60	0.99
FeO	2.77	2.50	1.76	1.84	2.26	2.07	2.88	2.60	2.58	2.73	2.62	2.33	4.51	1.67	2.04	1.94
MgO	16.30	16.91	17.25	16.87	17.58	18.75	16.77	17.52	17.16	18.43	17.42	17.04	19.85	18.40	18.18	18.45
CaO	22.08	22.94	24.45	24.25	24.00	21.57	22.73	22.46	21.43	22.05	21.77	21.97	15.32	23.83	23.25	23.67
Na_2O	0.58	0.22	0.18	0.41	0.49	0.33	0.51	0.40	0.62	–	–	0.62	0.70	–	–	–
Cr_2O_3	0.91	1.20	0.74	0.83	0.25	0.87	0.99	1.40	1.09	0.97	1.02	1.52	1.05	0.32	0.44	0.28
Sum	98.61	99.91	100.73	100.26	100.95	100.00	100.00	100.00	100.00	100.00	99.26	100.00	99.77	98.92	99.24	99.33

Table 3 (continued)

##	18	19	20	21	22	23	24	25	26	27	28	29	30	31	32	33
Formula coefficients																
Si	1.864	1.909	1.936	1.948	1.974	1.958	1.865	1.905	1.884	1.946	1.888	1.934	1.855	1.974	1.959	1.968
Ti	0.014	–	0.004	–	–	–	0.017	0.011	0.015	–	–	–	–	–	–	–
Al-IV	0.136	0.091	0.064	0.052	0.026	0.042	0.135	0.095	0.116	0.054	0.112	0.066	0.145	0.026	0.041	0.032
Al-VI	0.070	0.064	0.039	0.042	0.029	0.048	0.040	0.021	0.076	0.038	0.091	0.069	0.140	0.006	0.027	0.011
Fe	0.085	0.076	0.053	0.056	0.068	0.062	0.087	0.079	0.078	0.082	0.080	0.070	0.136	0.051	0.062	0.059
Mg	0.893	0.916	0.926	0.909	0.939	1.008	0.907	0.947	0.925	0.995	0.948	0.920	1.066	1.004	0.989	1.003
Ca	0.870	0.894	0.944	0.941	0.923	0.834	0.884	0.874	0.832	0.857	0.852	0.854	0.592	0.935	0.910	0.926
Na	0.041	0.015	0.013	0.029	0.034	0.023	0.036	0.028	0.044	–	–	0.043	0.049	–	–	–
Cr	0.026	0.034	0.021	0.024	0.007	0.025	0.028	0.040	0.031	0.028	0.030	0.043	0.030	0.009	0.013	0.008

Discussion

Compositional features of Cr-spinel

The composition of accessory Cr-spinel from lherzolite massifs regularly changes from lherzolites to harzburgites and dunites with a gradual increase in the Cr/Al ratio and concomitant decrease in the Mg/Fe ratio exhibiting a Cr–Al trend typical of ophiolites, abyssal peridotites, and mantle-derived xenoliths (Barnes and Roeder 2001). The degree of melting of mantle peridotites (Jaques and Green 1980) is considered one of the main factors of increasing Cr# value, as well as fO_2, pressure and the composition of coexisting phases (Ballhaus et al. 1991).

These compositional variations should most likely be related to partial melting, which is considered to be a main process during the uplift of mantle diapirs in rifts generating extensive basaltic volcanism (e.g., Ringwood 1975; Anderson 1989). The compositions of the accessory Cr-spinel from Uralian lherzolites and harzburgites on OSMA (olivine-spinel mantle association) diagram yield reasonable values of partial melting (10–30%) (Fig. 8a). The degree of melting estimated for Cr-spinel from dunites is higher than expected in the upper mantle (McKenzie and Blickle 1988), thus, the formation of the mineral assemblages of dunites requires alternative explanation (Kelemen et al. 1995).

The estimations of temperatures, pressure and oxygen fugacity based on the compositions of Cr-spinel and coexisting silicates (olivine, pyroxene), as well as the deformation structure of ultramafic rocks, correspond to those of the upper mantle conditions. They are within the ranges inferred for peridotite xenoliths, abyssal peridotites and mantle sections of other ophiolite complexes worldwide. (e.g. Ballhaus 1993; Arai and Ishimaru 2008; Ullah et al. 2020; Xiong et al. 2020).

Formation of accessory Cr-spinel in ultramafic rocks

Based on the morphological features, the Cr-spinel from peridotite bodies of the South Urals can be classified as follows: (i) the finest grains (lamellae and rods 0.1–10 μm in size) in silicates (type 1a) and similar (0.5–20 μm in size) grains along the boundaries of silicates and among neoblasts (type 1b) in peridotites and dunites, (ii) anhedral grains with branches and silicate inclusions (type 2) in lherzolites, (iii) vermicular, amoeboidal and skeletal grains in the assemblage with plagioclase (type 3) in Cr-spinel–plagioclase lherzolites and (iv) euhedral crystals in dunites (type 4a) and transitional subhedral crystals in harzburgites (type 4b). Types 1–3 are mostly characterized by the high or moderate Al_2O_3 content (30–50 wt.%) and type 4 exhibits high-Cr spinel (Cr# = 0.75–0.8).

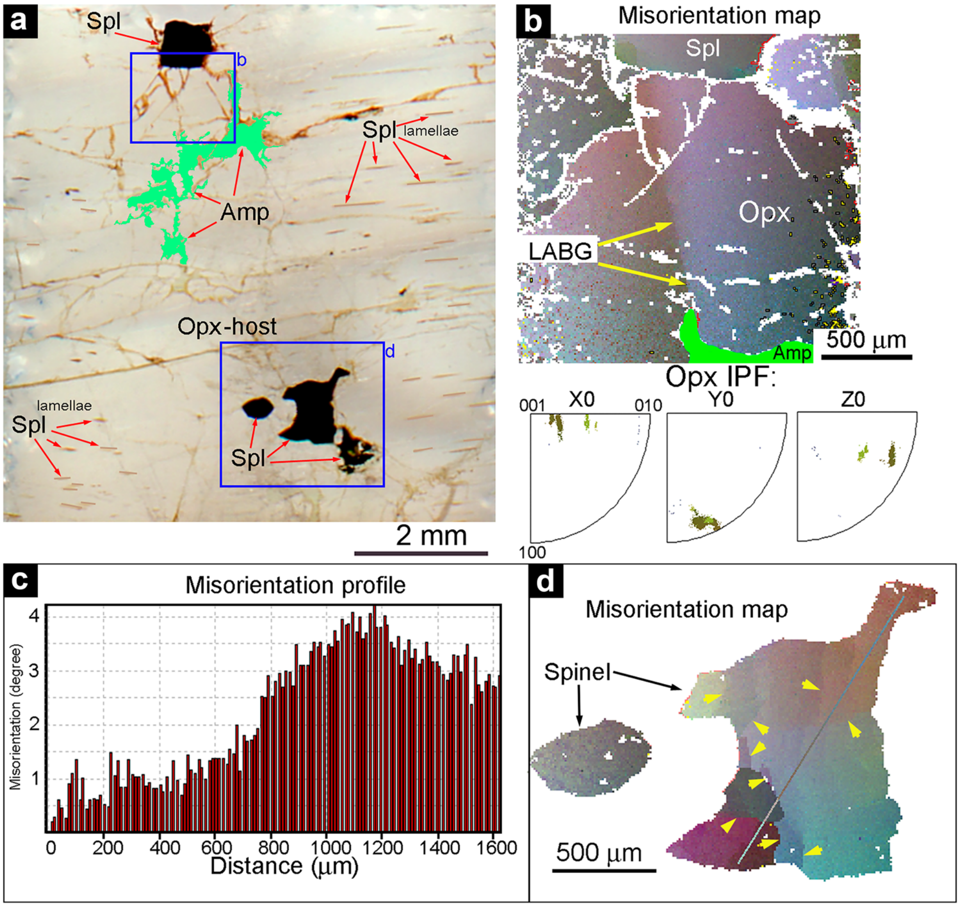

Fig. 9 Morphology and microstructure of Cr-spinel in deformed enstatite from Central Kraka massif (sample K0852): **a** general view (scanned image); **b** pargasite along low-angle grain boundary (LAGB) in host enstatite; **c** misorientation profile through a holly-leaf Cr-spinel grain shown in **d**; **d** misorientation map of large holly-leaf Cr-spinel grain with a domain substructure (yellow arrows indicate LAGBs)

Types 1a and 1b Cr-spinel

Tiny Cr-spinel of types 1a and 1b is observed in (1) areas of intense deformation inside olivine grains (Fig. 6a), (2) areas composed of fine-grained neoblasts of enstatite, diopside and forsterite (Fig. 6c, d) and (3) sliding plane or sub-boundaries of plastically deformed enstatite (Fig. 6b). Therefore, the formation of newly-formed Cr-spinel crystals is related to lattice defects in olivine and orthorhombic pyroxene.

In the areas of intense deformation (case 1), the Cr-spinel grains are regularly confined to kink-band zones (Saveliev 2019; Saveliev et al. 2021) suggesting that the Cr-spinel rods and locally associated amphibole could have formed from segregated ions of trace elements (Cr and Al for Cr-spinel; Ca, Al, Na and H for pargasite) on defects of the olivine lattice. Our microstructural data support this suggestion (Fig. 11).

The most abundant case 2 is probably caused by fragmentation of primary enstatite I due to intense recrystallization, which resulted in the formation of newly-formed crystals of trace element-depleted enstatite II, diopside, forsterite, pargasite and Cr-spinel (Fig. 6d).

In the case 3, the Cr-spinel grains form in the internal part of the deformed crystal along with diopside and/or pargasite (Saveliev and Musabirov 2019; Saveliev et al. 2021). The lamellae in plane (100) could have formed similarly to the formation of stacking faults in sliding plane as shown in (Boland 1974; McLaren and Etheridge 1976; Kirby and Etheridge 1981; Van Duysen et al. 1985). The lamellae at a low-angle boundary, which divides the misoriented blocks of curved enstatite crystals, could be a result of segregation of trace atoms on lattice defects and misalignments in host mineral.

In addition to the above occurrence of Cr-spinel neoblasts, they are also observed inside the newly formed diopside grains included into plastically deformed enstatite (Saveliev et al. 2021). In this case, two scenarios of their origin are possible. From one hand, the presence of complex Cr-spinel–diopside and Cr-spinel–diopside–pargasite lamellae in enstatite (e.g. Fig. 6b) indicates their solid-phase origin. From the other hand, the assemblage and gradual transitions between anhedral aggregates of pargasite and its lamellae indicate their possible formation as a result of deformation-induced diffuse decomposition of enstatite with further melting of newly formed amphibole. One possible mechanism is related to friction melting, which is caused by contribution of energy in form of heat from deformed minerals on sliding surface (Spray 1988, 1992).

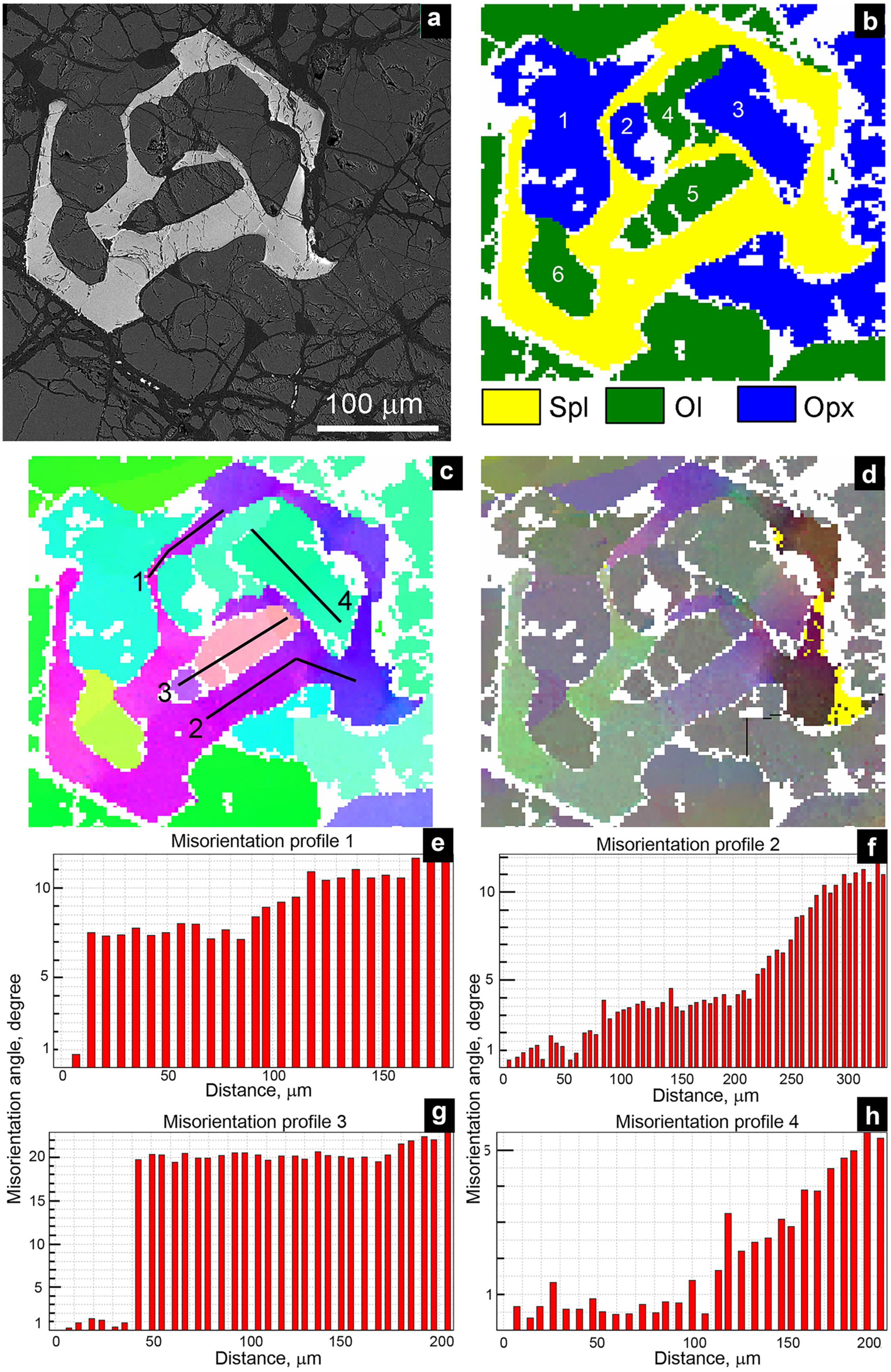
a
100 µm
b
1
2
3
4
5
6
Spl
Ol
Opx
c
1
2
3
4
d
Misorientation profile 1
e
Misorientation angle, degree
10
5
1
0
50
100
150
Distance, µm
Misorientation profile 2
f
Misorientation angle, degree
10
5
1
0
50
100
150
200
250
300
Distance, µm
Misorientation profile 3
g
20
15
10
5
1
0
50
100
150
200
Distance, µm
Misorientation profile 4
h
5
1
0
50
100
150
200
Distance, µm

◂**Fig. 10** Microstructure of a skeletal Cr-spinel grain associated with olivine and orthopyroxene from Nurali massif (sample N0258): **a** BSE image, **b** phase map, **c** IPF map in plane normal to X axis (1–4 – misorientation profiles), **d** misorientation map, **e–h** misorientation profiles shown in **c**

It should be noted that similar newly-formed tiny spinels in the association with pyroxenes were described in lherzolites of the Syum-Keu massif in the Polar Urals (Savelieva et al. 2016). The authors noted similar patterns in the localization of the spinel segregations and the composition of coexisting minerals: a decrease in Cr and Al in pyroxene grains from core to rims, depletion of these elements in neoblasts compared to porphyroclasts, the presence of pargasite chains parallel to the plastic flow zones, confinement of spinel precipitations to areas of intense deformation of silicate grains and recrystallization zones. The authors of the cited work proposed the solid-phase decomposition of pyroxenes as the main mechanism for the formation of newly formed spinels (Savelieva et al. 2016) that is consistent with our interpretation (Saveliev et al. 2017, 2021).

Types 2 and 3 Cr-spinel

The formation of anhedral Cr-spinel (e.g. Fig. 4c–f), as well as the euhedral crystals with fine holly leaves (e.g. Figs. 4c, d and 5c, d), was previously considered to be related to the restitic origin of host peridotites (Mercier and Nicolas 1975; Noller and Carter 1986) and was structurally substantiated, because this morphology can better be explained by morphological changes as a result of solid-phase processes. During the onset and evolution of the melt/rock interaction model, the reaction origin of anhedral Cr-spinel became widely accepted and was explained by heterogeneous dilution (resorption) of primary igneous euhedral crystals (e.g., Johnson 2012).

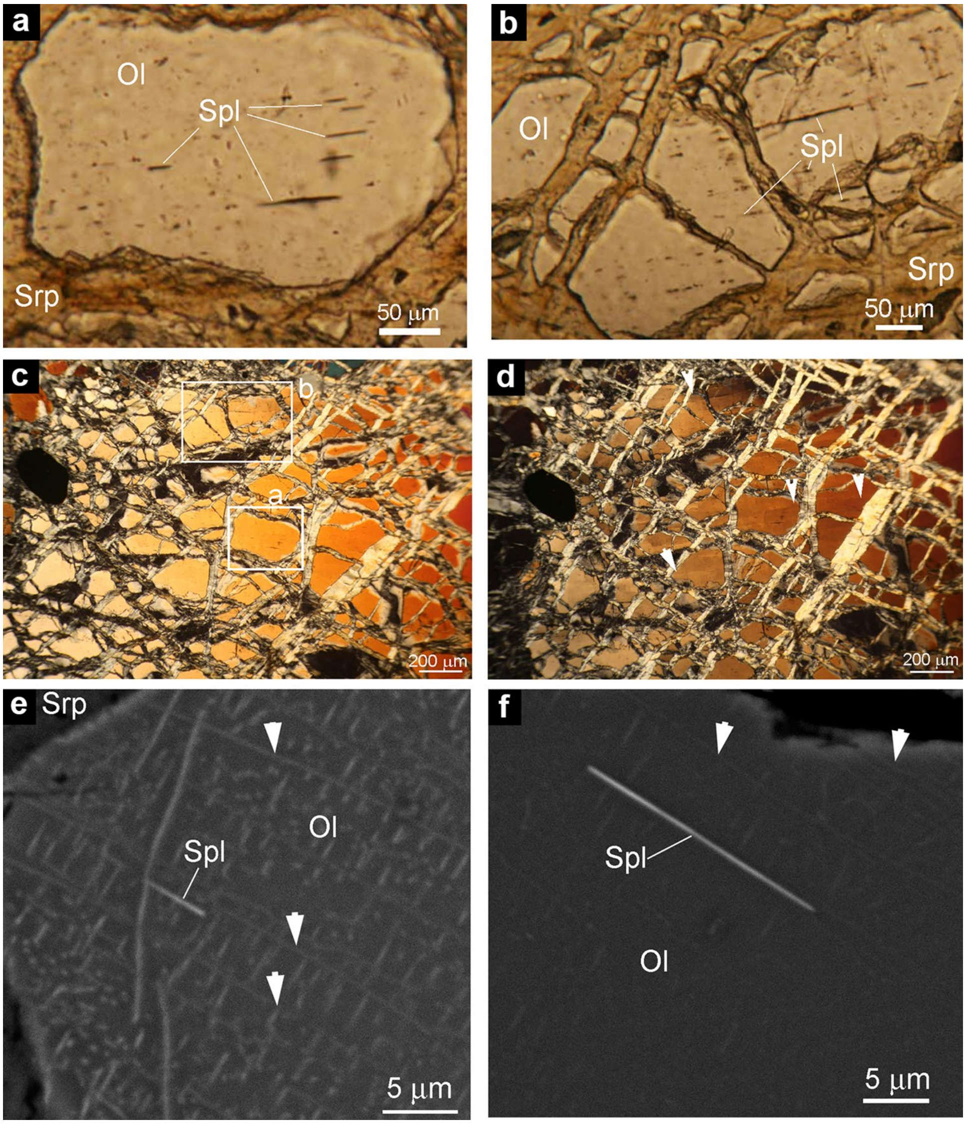

Fig. 11 Parallel Cr-spinel rods in olivine grains from Nurali massif (sample N0260, dunite): **a** and **b** polarized transmitted light, **c** and **d** cross-polarized transmitted light, **e** and **f** BSE images of samples subjected to oxidative decoration of dislocations. White arrows in Fig. **d–f**, tilt walls

Previously (Saveliev et al. 2017, 2021), we provided evidences of numerous gradual transitions from fine rods and plates to larger "anhedral" crystals completely enclosed in high-temperature silicates (olivine and orthopyroxene) without any visible presence of fluid (melt) agents. In this case, the Cr-spinel could not enclose the silicate fragments during crystallization from melt due to following reasons. First, Cr-spinel crystallizes first or simultaneously with olivine from parental picritic or boninitic melts or due to a reaction responsible for the formation of ophiolitic dunites and harzburgites. In this case, the magmatic or reaction magmatic origin of Cr-spinel crystals contradicts the presence both of orthopyroxene and olivine inclusions (Fig. 10). Second, the presence of finest Cr-spinel tracks, which divide the small fragments of silicates from the rest of the large crystal (Figs. 6f and 10), indicates that the Cr-spinel is later mineral with a lower crystallization temperature (from the viewpoint of magmatic origin).

Our microstructural studies of holly-leaf crystals (Figs. 9 and 10) revealed the structural heterogeneities of silicates, which are enclosed by Cr-spinel grains. The origin of most low-angle boundaries is interpreted as a result of plastic deformation (translation sliding). The Cr-spinels demonstrate both anhedral and euhedral habits. The misorientation angle of the intracrystalline domains is typically < 10° with gradual transitions towards boundaries. In our opinion, this can be explained by syn-deformation growth of Cr-spinel grain following one of the mechanisms, which have been suggested for the crystallization of porphyroblasts in metamorphic rocks (Bell et al. 1986; Prior 1987; Gaidies et al. 2017). The necessary amount of Cr and Al was sourced from pyroxenes (olivine, to lesser extent), which underwent deformation-induced decay during plastic flow (Figs. 3, 6 and 9–11 and Figs. in Saveliev et al. 2017, 2021).

It should also be noted that the process of formation (growth) of new spinel grains due to the decomposition of the enstatite precursor is sometimes recorded in lherzolite microstructures. It is expressed either in "core-mantle" structures (Fig. S6a, b), when the "mantle" is represented by neoblasts of spinel, diopside, pargasite, forsterite, and enstatite where phase boundaries are established only by EDS mapping (Fig. S6c–g), or in the presence of contrastly zoned anhedral spinel grains at the contact with deformed enstatite (Fig. S6h–i), where the grain edges adjacent to pyroxene are Cr-rich whereas the grain volume and edges next to olivine inclusions are of high-Al composition. In the rim of enstatite porphyroclasts, the formation of the smallest grains of spinel, diopside and pargasite is noted (Fig. S6j). For comparison, it should be noted that in dunites we typically observed an equilibrium association of high-Mg forsterite and high-Cr spinel.

In many cases, the anhedral and subhedral Cr-spinel exhibits a spatial link with plagioclase or its alteration products. The genesis of Cr-spinel–plagioclase lherzolites is most likely explained by either (i) crystallization from percolating partial melt through a peridotite restite (Nicolas 1986; Nicolas and Dupuy 1984; Rampone et al. 2010) or (ii) phase transition during the uplift of mantle material from the depth of spinel facies to the stability depth of the plagioclase-bearing assemblages (Piccardo et al. 1990; Rampone et al. 1993; Shimizu et al. 2008; Pirnia et al. 2018). The first scenario implies that the rock should contain both restitic (Cr-spinel and olivine) and basaltic (plagioclase and clinopyroxene) components. This was observed in a few samples (Fig. 7e, f), therefore, the first scenario can only be accepted as a partial explanation in some specific cases.

Fig. 12 Model of formation of ophiolitic dunite bodies with accessory ▶ euhedral Cr-spinel grains and various types of chromitite bodies: **a** initial stage – the formation of dunite zones of plastic flow in mantle peridotite (thin section scale), the concurrent processes include deformation-induced decomposition of enstatite, the release of newly-formed Cr-spinel grains, and simultaneous precipitation of Cr-spinel on defects in enstatite and olivine; **b** early stage – the formation of wide zones of localized plastic flow (of dunites) and the segregation of disseminated fine-grained chromitite bodies inside them – concordant tabular deposits; **c** advanced stage – the complication of structure of dunite zones due to segregation of Cr-spinels, leading to the grain impingement and their enlargement caused by annealing. As a result, chromitite produces a strong rheological response and is separated from the mobile dunite zone although the ore bodies are trapped in the branches ("apophyses") or inside isolated dunite envelopes (with possible formation of concordant, subconcordant, discordant podiform deposits)

In most studied rocks, however, the Cr-spinel occupies the axial part of the aggregates. The primary aggregates exhibit skeletal morphology of Cr-spinel and its central position (Fig. 7a, b) resembles the symplectitic intergrowths, which are typically interpreted as a decay of the precursor minerals upon the decrease in pressure and/or temperature (e.g., Gaidies et al. 2017). Symplectites, as a rule, are finer-grained relatively to the precursor phase; however, this term is sometimes applied for relatively coarse-grained intergrowths comparable with the Uralian plagioclase-chromite aggregates by their size (Shimizu et al. 2008).

The second interpretation scenario requires the presence of a high-pressure precursor, which is enriched in Si, Cr, Al, Ca, Mg and Fe and would decompose to Cr-spinel + plagioclase assemblage during the pressure drop. The mass balance calculations for the samples of the Nurali massif yielded an average weighted chemical composition of a probable precursor (wt%): 29.03 SiO_2, 32.06 Al_2O_3, 13.99 Cr_2O_3, 5.54 MgO, 9.58 CaO, 8.03 FeO and 1.68 Na_2O (Saveliev 2019). The atomic ratios between O and Si in a primary mineral are significantly distinct from pyroxene ratios and most similar to those of garnet, however, only if Cr occupies position X (i.e., it occurs in two valent state), which is possible only at significant depths and/or under conditions of low oxygen

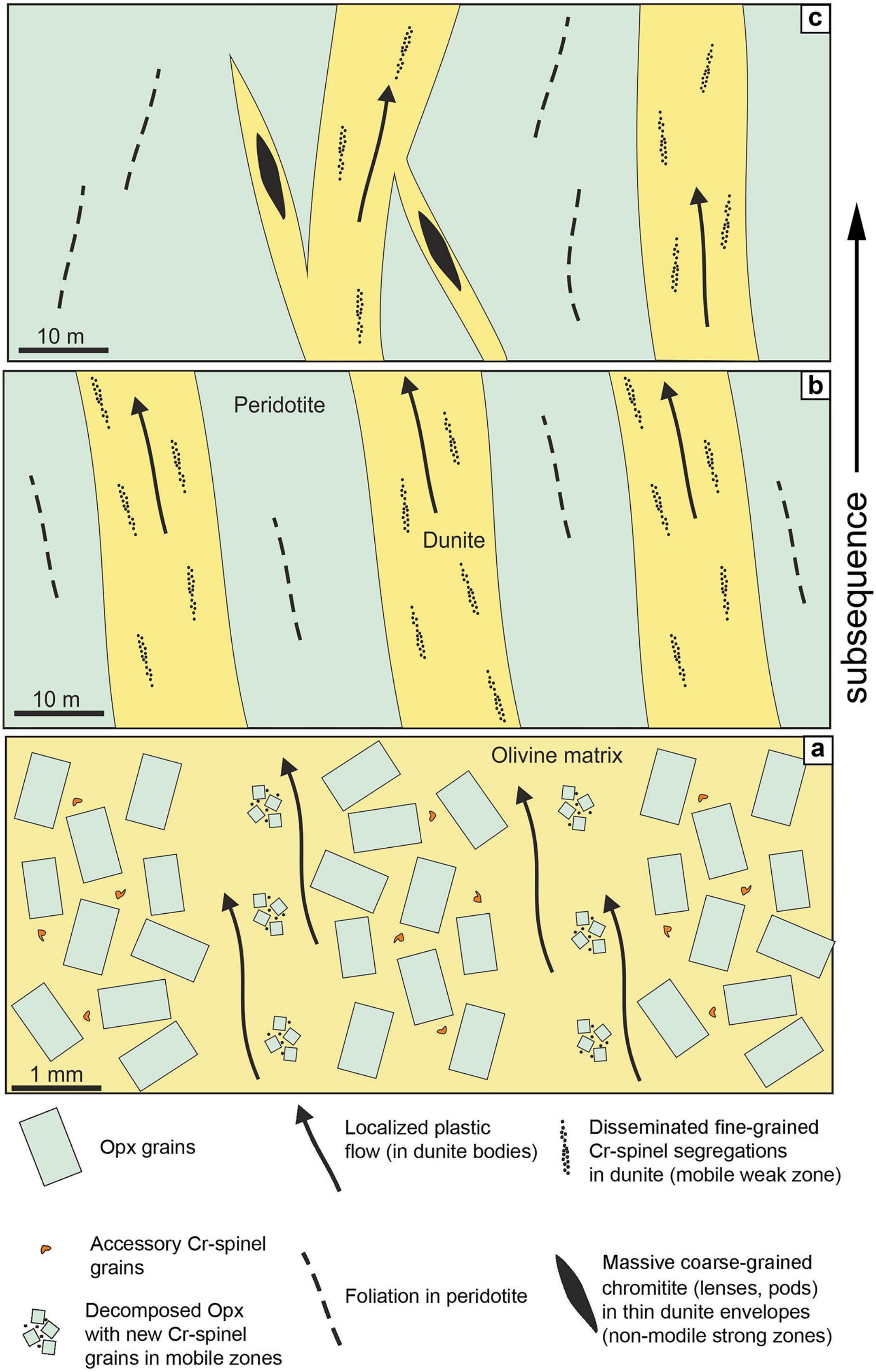
c
10 m
b
Peridotite
Dunite
10 m
a
Olivine matrix
1 mm
subsequence
Opx grains
Localized plastic flow (in dunite bodies)
Disseminated fine-grained Cr-spinel segregations in dunite (mobile weak zone)
Accessory Cr-spinel grains
Decomposed Opx with new Cr-spinel grains in mobile zones
Foliation in peridotite
Massive coarse-grained chromitite (lenses, pods) in thin dunite envelopes (non-modile strong zones)

fugacity (e.g. Ryabchikov et al. 1981). Using an algorithm of (Grew et al. 2013), the composition of the probable primary phase, which would undergo decompression decomposition during the uplift of lherzolites in a mantle diapir structure, was recalculated to garnet $(Cr_{0.833}Ca_{0.775}Mg_{0.622}Fe_{0.466}Na_{0.246})_{2.942}Al_{2.083}(Si_{2.190}Al_{0.810})_{3.00}O_{12.00}$.

Thus, we suggest the following scenarios of the formation of the macroscopic anhedral Cr-spinel grains: (i) syndeformation growth in close interaction with host silicates – for the holly leaf grains closely associated with olivine and orthopyroxene, (ii) decompression decay of the precursor (garnet?) – for the anhedral grains intergrown with plagioclase and (iii) crystallization due to partial melting and percolating melts – for the anhedral and subhedral grains in assemblage with plagioclase and clinopyroxene.

Type 4 Cr-spinel and rheomorphic model

Within the widely accepted mantle/rock interaction model, the crystallization of euhedral Cr-spinel grains in dunites (e.g. Fig. 4b) is considered as a result of reaction between migrating primitive melts and mantle peridotite (Kelemen 1990; Arai and Yurimoto 1994; Zhou et al. 1996). The main problems of this model include: (i) the absence of a sufficient space for convection and precipitation of abundant Cr-spinel from melt and (ii) instant removal of Cr-spinel and forsterite-producing melt residues from a channel. In addition, the crystallization of Cr-spinel after the dissolution of pyroxenes cannot provide more than a few vol % of grains in rocks. The formation of chromite ores, which are occur in dunites only, requires another additional mechanism of chromite accumulation.

We suggest another formation of euhedral Cr-spinel in dunites (Saveliev 2021; Saveliev and Fedoseev 2019). The Cr-spinel crystals form inside the solid-phase flow of mantle material as a result of minimization of intergranular energy, which excessively accumulates in anhedral Cr-spinel from peridotites. As shown in this and other works (McElduff and Stumpfl 1991; Pushkarev et al. 2015; Borisova et al. 2012; Johan et al. 2017; Miura et al. 2012), the Cr-spinel from dunites and chromitites contains numerous inclusions of silicate and other exotic phases (pargasite, phlogopite, etc.), the presence of which is hard to explain by magmatic models.

In contrast, the structural–mineralogical features are logically explained by a rheomorphic model, according to which the source material for the formation of chromite ores were primitive lherzolites of the upper mantle. This material is redistributed as a result of interaction of two main processes: ascending plastic flow of mantle material and partial melting.

The critical zone of transition from wall peridotite to dunite body is a zone of most intense flow (Saveliev and Fedoseev 2019) due to weakest rheological properties of olivine (Karato 2008; Yamamoto et al. 2008). The formation of various microinclusions in olivine and Cr-spinels is a result of deformation-induced segregation of trace elements. This process leads to vanishing pyroxenes and formation of additional Cr-spinel neoblasts in newly formed dunite (Saveliev et al. 2017, 2021).

The movement in ascending mantle flow results in the formation of dunite bodies with a thickness varying from few meters to few hundreds of meters, which enclose significant amount of disseminated Cr-spinel (Fig. 12a). Progressive transportation of dunites leads to their stratification and formation of Cr-spinel segregations. As long as the Cr-spinel grains exhibit no contacts, their segregations are fine-grained disseminated ores, which are concordant with internal structure of the flow where the ore grains are separated from each other by dunite envelopes (Fig. 12b).

When segregation results in attachment of the grains, they will expand due to minimization of the grain-boundary energy (e.g., Karato 2008) that is similar to Ostwald ripening (Lifshits and Pitaevskii 1979). The expansion of grain sizes leads to a sharp change in the rheological properties of the ore aggregates and slower movement inside the mobile dunite flow. At the same time, due to macroscopic sizes of the ore aggregates, the dunite envelope keeps them unmixed with ambient peridotite. This can be responsible for the formation of podiform bodies of massive coarse-grained chromitites (Fig. 12c).

Therefore, in our model, a range of initial dunites with the variable proportions of chromite from accessory Cr-spinel to disseminated fine-grained chromitite and up to massive coarse-grained chromitite could successively form due to stationary mantle plastic flow under decompression regime. A wide variation in the size of ore bodies can be explained by variable efficiency of plastic flow and synchronous partial melting.

Conclusions

Accessory Cr-spinel of the peridotite massifs of the South Urals can be subdivided into several types with corresponding formation mechanisms. The finest Cr-spinel lamellae and rods in silicates (type 1a) and the grains along the silicate boundaries and among the silicate neoblasts (type 1b) formed as a result of deformation-induced segregation of trace elements on the defects of the olivine lattice. The anhedral holly-leaf Cr-spinel grains with the inclusions of silicates (type 2) in lherzolites are interpreted as a result of synkinematic growth in deforming silicate matrix.

The formation of Cr-spinel associated with plagioclase (type 3) can be related to various processes: skeletal Cr-spinel might form during decompression decay of a high-pressure precursor (garnet?) (type 3a) whereas subhedral Cr-spinels might crystallize from percolating melts or as a result of reaction of these melts with restite (type 3b). The euhedral Cr-spinel crystals in dunites (type 4) most likely formed during cyclic crystallization/recrystallization in the continuous plastic flow under high pressure and temperature conditions. Further solid-phase redistribution of the Cr-spinel grains inside dunites led to the formation of the chromitite bodies.

The main trends of chemical changes in accessory Cr-spinel include the monotonous increase in Cr# and decrease in Mg# values from lherzolites to harzburgites and dunites. This reflects a well known trend related to the partial melting of mantle material and concentration of Cr-spinel in restite, which is also subjected to the solid-phase differentiation.

Supplementary Information The online version contains supplementary material available at https://doi.org/10.1007/s00710-022-00791-1.

Acknowledgements This work was supported by the Russian Science Foundation, grant #22-17-00019, https://rscf.ru/project/22-17-00019/ and was carried out using facilities of the Center for the Collective Use of the IMSP RAS "Structural and Physico-Mechanical Studies of Materials" and Geomodel and Nanofotonika Resource Centers of St. Petersburg State University. The authors are grateful to Mikhail Lozhkin for help in preparation of samples for microstructural studies and to Alexey I. Chernyshov and Igor S. Chaschukhin who provided fresh Kempirsai peridotite samples to study. We also very grateful to M.A.Yudovskaya and an anonymous reviewer for useful comments that allowed us to significantly improve the manuscript. Field work carried out partly at the expense of the State contract no. FMRS-2022-0011.

Author contributions Saveliev D.E. – field work, sample preparation, optical microscope study, SEM/EMPA study, manuscript writing; Shilovskykh V.V. – sample preparation, EBSD study and interpretation; Makatov D.K. – field work, sample preparation, optical microscope study; Gataullin R.A. – field work, sample preparation, optical microscope study.

Funding This study was supported by Russian Science Foundation, grant #22–17-00019, https://rscf.ru/project/22-17-00019/ and field work was performed as part of government contract #FMRS-2022–0011.

Availability of data and material Partially data is available in ESM.

Code availability Not applicable to this manuscript.

Declarations

Conflicts of interest No conflict of interest.

References

Ahmed AH, Moghazi AKM, Moufti MR, Dawood YH, Ali KA (2016) Nature of the lithospheric mantle beneath the Arabian Shield and genesis of Al-spinel micropods: Evidence from the mantle xenoliths of Harrat Kishb, Western Saudi Arabia. Lithos 240–243:119–139. https://doi.org/10.1016/j.lithos.2015.11.016

Anderson DL (1989) Theory of the Earth. Blackwell scientific publication, Boston, Oxford, London, Edinburgh, Melburn

Arai S (1980) Dunite-harzburgite-chromitite complexes as refractory residue in the Sangun-Yamaguchi zone, western Japan. J Petrol 21:141–165

Arai S (1994) Characterization of spinel peridotites by olivine-spinel compositional relationships: Review and interpretation. Chem Geol 113:191–204

Arai S, Ishimaru S (2008) Insights into petrological characteristics of the lithosphere of mantle wedge beneath arcs through peridotite xenoliths: a review. J Petrol 49:665–695

Arai S, Miura M (2016) Formation and modification of chromitites in the mantle. Lithos 264:277–295. https://doi.org/10.1016/j.lithos.2016.08.039

Arai S, Yurimoto H (1994) Podiform chromitites from the Tari-Misaka ultramafic complex, southwestern Japan, as a melt mantle interaction products. Econ Geol 89:1279–1288

Auge T (1987) Chromite deposits in the northern Oman ophiolite: mineralogical constraints. Mineral Deposita 22:1–10

Ballhaus C (1993) Redox states of lithospheric and asthenospheric upper mantle. Contrib Miner Petrol 114:331–348

Ballhaus C (1998) Origin of the podiform chromite deposits by magma mingling. Earth Planet Sci Lett 156:185–193

Ballhaus C, Berry R, Green D (1991) High pressure experimental calibrationof the olivine-orthopyroxene-spinel oxygen geobarometer: implication for the oxydation state of the upper mantle. Contrib Miner Petrol 107:27–40

Barnes S, Roeder P (2001) The range of spinel compositions in terrestrial mafic and ultramafic rocks. J Petrol 42:2279–2302. https://doi.org/10.1093/petrology/42.12.2279

Bazylev BA (2003) Petrological and geochemical evolution of mantle matter in lithosphere: comparative study of oceanic and alpine-type spinel peridotites. Ph.D. thesis, Moscow: Vernadsky Institute of geochemistry and analytical chemistry (in Russian)

Bell TH, Fleming PD, Rubenach MJ (1986) Porphyroblast nucleation, growth and dissolution in regional metamorphic rocks as a function of deformation partitioning during foliation development. J Metamorph Geol 4:37–69

Boland JN (1974) Lamellar structures in low calcium orthopyroxenes. Contrib Miner Petrol 47:215–222

Borisova AY, Ceuleneer G, Kamenetsky VS, Arai S, Béjina F, Abily B, Bindeman IN, Polvé M, De Parseval P, Aigouy T, Pokrovski GS (2012) A new view on the petrogenesis of the Oman ophiolite chromitites from microanalyses of chromite-hosted inclusions. J Petrol 53:2411–2440

Boudier F, Nicolas A (1985) Harzburgite and lherzolite subtypes in ophiolitic and oceanic environments. Earth Planet Sci Lett 76:84–92

Brey GP, Köhler T (1990) Geothermobarometry in 4-phase lherzolites: 2. New thermobarometers, and practical assessment of existing thermobarometers. J Petrol 31:1353–1378

Chashchukhin IS, Votyakov SL (2009) Behavior of iron-group elements, oxybarometry, and genesis of unique chromite deposits in the Kempirsai massif. Geol Ore Deposits 51:123–138

Dick HJB, Bullen T (1984) Chromian spinel as a petrogenetic indicator in abyssal and Alpine-type peridotites and spatially associated lavas. Contrib Miner Petrol 86:54–76

Fabries J (1979) Spinel-olivine geothermometry in peridotites from ultramafic complexes. Contrib Miner Petrol 69:329–336

Gaidies F, Milke R, Heinrich W, Abart R (2017) Metamorphic mineral reactions: Porphyroblast, corona and symplectite growth. Eur Mineral Union Notes Mineral 16:469–540. https://doi.org/10.1180/EMU-notes.16.14

Green DH, Falloon TJ (1998) Pyrolite: a Ringwood concept and its current expression. In: Jackson I (ed) The Earth's mantle composition, Structure and Evolution 7. Cambridge University Press, Cambridge, pp 311–378

Grew ES, Locock AJ, Mills S, Galuskina IO, Galuskin EV, Hålenius U (2013) Nomenclature of the garnet supergroup. Am Miner 98:785–811

Jaques AL, Green DH (1980) Anhydrous melting of peridotite at 0–15 kbar pressure and the genesis of tholeiitic basalts. Contrib Miner Petrol 73:287–310

Johan Z, Martin RF, Ettler V (2017) Fluids are bound to be involved in the formation of ophiolitic chromite deposits. Eur J Mineral 29:543–555

Johnson C (2012) Podiform chromite at Voskhod, Kazakhstan. Ph.D. thesis, Cardiff University

Kamenetsky VS, Crawford AJ, Meffre S (2001) Factors controlling chemistry of magmatic spinel: an empirical study of associated olivine, Cr-spinel and melt inclusions from primitive rocks. J Petrol 42:655–671

Karato S-I (2008) Deformation of Earth Materials. Cambridge University Press, An introduction to the rheology of Solid Earth

Kelemen PB (1990) Reaction between ultramafic rock and fractionating basaltic magma. I. Phase relations, the origin of calc-alkaline magma series, and the formation of discordant dunite. J Petrol 31:51–98

Kelemen PB, Shimizu N, Salters VJM (1995) Extraction of mid-ocean-ridge basalt from the upwelling mantle by focused flow of melt in dunite channels. Nature 375:747–753

Kirby SH, Etheridge MA (1981) Exsolution of Ca pyroxene from orthopyroxene aided by deformation. Phys Chem Miner 7:105–109

Leblanc M (1980) Chromite growth, dissolution and deformation from a morphological view point: SEM investigations. Miner Deposita 15:201–210

Leblanc M (1995) Chromitite and ultramafic rock compositional zoning through a paleotransform fault, Poum, New Caledonia. Econ Geol 90:2028–2039

Lifshits EM, Pitaevskii LP (1979) Physical kinetics. Main edition of physical and mathematical literature, Moscow (in Russian)

Matsumoto I, Arai S (2001) Morphological and chemical variations of chromian spinel in dunite-harzburgite complexes from the Sangun zone (SW Japan): implications for mantle/melt reaction and chromitite formation processes. Mineral Petrol 73:305–323

McElduff B, Stumpfl EF (1991) The chromite deposits of the Troodos Complex, Cyprus: evidence for the role of a fluid phase, accompanying chromite formation. Miner Deposita 26:307–318

McKenzie D, Bickle MJ (1988) The volume and composition of melt generated by extension of the lithosphere. J Petrol 29:625–679. https://doi.org/10.1093/petrology/29.3.625

McLaren AC, Etheridge MA (1976) A transmission electron microscope study of naturally deformed orthopyroxene. I. Slip mechanisms. Contrib Miner Petrol 57:163–177

Mercier JC, Nicolas A (1975) Textures and fabrics of upper mantle peridotites as illustrated by basalt xenoliths. J Petrol 16:454–487

Miura M, Arai S, Ahmed AH, Mizukami T, Okuno M, Yamamoto S (2012) Podiform chromitite classification revisited: a comparison of discordant and concordant chromitite pods from Wadi Hilti, northern Oman ophiolite. J Asian Earth Sci 59:52–61

Morishita T, Andal ES, Arai S, Ishida Y (2006) Podiform chromitites in the lherzolite-dominant mantle section of the Isabela ophiolite, the Philippines. The Island Arc 15:84–101. https://doi.org/10.1111/j.1440-1738.2006.00511.x

Moutte J (1982) Chromite deposita of the Tiebaghi ultramafic massif, New Caledonia. Econ Geol 77:576–591

Nicolas A (1986) Structure and petrology of peridotites: clues to their geodynamic environment. Rev Geophys 24:875–895

Nicolas A, Bouchez JL, Boudier F, Mercier JC (1971) Textures, structures and fabrics due to solid state flow in some European lherzolites. Tectonophysics 12:55–86

Nicolas A, Dupuy C (1984) Origin of ophiolitic and oceanic lherzolites. Tectonophysics 110:177–187

Nielson-Pike JE, Schwarzman EC (1977) Classification of textures in ultramafic xenoliths. J Geol 85:49–61

Noller JS, Carter B (1986) The origin of various types of chromite schlieren in the Trinity peridotite, Klamath Mountains, California, In: Carter B (ed) Metallogeny of basic and ultrabasic rocks. Theophrastus Publications, pp 151–178

Ono A (1983) Fe-Mg partioning between spinel and olivine. J Japanese Assoc Miner Petrol Econ Geol 78:115–122

Ozawa K (1983) Evaluation of Olivine-Spinel Geothermometry as an Indicator of Thermal History for Peridotites. Contrib Miner Petrol 82:52–65

Parkinson IJ, Pearce JA (1998) Peridotites from the Izu–Bonin–Mariana forearc (ODP Leg 125): evidence for mantle melting and melt–mantle interaction in a supra-subduction zone setting. J Petrol 39:1577–1618

Passchier CW, Trouw RAJ (2005) Microtectonics. 2nd, Revised and Enlarged Edition. Springer-Verlag Berlin Heidelberg

Pavlov NV, Kravchenko GG, Chuprynina II (1968) Chromitites of Kempirsai pluton. Nauka, Moscow (in Russian)

Piccardo GB, Rampone E, Vannucci R (1990) Upper mantle evolution during continental rifting and ocean formation: evidence from peridotite bodies of the Western Alpine - Northern Apennine system. Mémoires De La Société Géologique De France 156:323–333

Pirnia T, Saccani E, Arai S (2018) Spinel and plagioclase peridotites of the Nain ophiolite (Central Iran): Evidence for the incipient stage of oceanic basin formation. Lithos 310–311:1–19. https://doi.org/10.1016/j.lithos.2018.04.001

Prior DJ (1987) Syntectonic porphyroblast growth in phyllites: textures and processes. J Metamorph Geol 5:27–39

Puchkov VN (1997) Structure and geodynamics of the Uralian orogen. In Orogeny Through Time. Published by The Geological Society London. Ed. J.-P. Burg and M. Ford., pp 201–236

Pushkarev EV, Kamenetsky VS, Morozova AV, Khiller VV, Glavatskykh SP, Rodemann T (2015) Ontogeny of ore Cr-spinel and composition of inclusions as indicators of the pneumatolytic–hydrothermal origin of PGM-bearing chromitites from Kondyor massif, the Aldan Shield. Geol Ore Deposits 57:352–380

Putirka KD (2008) Thermometers and barometers for volcanic systems. Rev Mineral Geochem 69:61–120

Rampone E, Piccardo GB, Vannucci R, Bottazzi P, Ottolini L (1993) Subsolidus reactions monitored by trace element partitioning: the spinel- to plagioclase-facies transition in mantle peridotites. Contrib Miner Petrol 115:1–17

Rampone E, Vissers RLM, Poggio M, Scambelluri M, Zanetti A (2010) Melt migration and intrusion during exhumation of the Alboran lithosphere: the Tallante mantle xenolith record (Betic Cordillera, SE Spain). J Petrol 51:295–325

Ringwood AE (1975) Composition and structure of the Earth's mantle. McGraw-Hill, New York

Roeder RL, Campbell IH, Jamieson HE (1979) A re-evaluation of the olivine-spinel geothermometer. Contrib Miner Petrol 68:325–334

Rollinson H (2005) Chromite in the mantle section of the Oman ophiolite: a new genetic model. The Island Arc 14:542–550

Ryabchikov ID, Green DH, Wall VJ, Brey GP (1981) The oxidation state of carbon in the reduced-velocity zone. Geochem Int 18:148–158

Saveliev DE (2018) Kraka ultramafic massifs (the Southern Urals): features of structure and composition of peridotite-dunite-chromitite assemblages Ufa: Bashkirian encyclopedia, 304 p. (in Russian with English Summary)

Saveliev DE (2019) Morphological and compositional features of chromian spinel from mantle ultramafic rocks of the Nurali massif (South Urals). Mineralogiya 5:3–18. (in Russian). https://doi.org/10.35597/2313-545X-2019-5-4-1

Saveliev DE (2021) Chromitites of the Kraka ophiolite (South Urals, Russia): geological, mineralogical and structural features. Miner Deposita 56(6):1111–1132. https://doi.org/10.1007/s00126-021-01044-5

Saveliev DE, Fedoseev VB (2019) Solid-state redistribution of mineral particles in the upwelling mantle flow as a mechanism of chromite concentration in the ophiolite ultramafic rocks (by the example of Kraka ophiolite, the Southern Urals). Georesources 21:31–46. https://doi.org/10.18599/grs.2019.1.31-46

Saveliev DE, Musabirov II (2019) About mechanisms of the chromian spinel crystal formation induced by plastic deformation of enstatite grains in mantle peridotites. Zapiski RMO (Proc Russian Miner Soc) 148:28–49. (in Russian). https://doi.org/10.30695/zrmo/2019.1482.02

Saveliev DE, Puchkov VN, Sergeev SN, Musabirov II (2017) Deformation-induced decomposition of enstatite in mantle peridotite and its role in partial melting and chromite ore formation. Doklady Earth Sci 476:1058–1061. https://doi.org/10.1134/S1028334X17090161

Saveliev DE, Shilovskikh VV, Sergeev SN, Kutyrev AV (2021) Chromian spinel neomineralisations and the microstructure of plastically deformed ophiolitic peridotites (Kraka massifs, Southern Urals, Russia). Mineral Petrol 115(4):411–430. https://doi.org/10.1007/s00710-021-00748-w

Saveliev DE, Snachev VI, Savelieva EN, Bazhin EA (2008) Geology, petrogeochemistry, and chromite content of gabbro-ultramafic massifs of the South Urals. Ufa: DizaynPoligrafServis (in Russian)

Savelieva GN (1987) Gabbro-ultramafic complexes of the Uralian ophiolites and their analogs in the present-day oceanic crust. Nauka, Moscow (in Russian)

Savelieva GN, Batanova VG, Sobolev AV (2016) Pyroxene–Cr-spinel exsolution in mantle lherzolites of the Syum-Keu ophiolite massif (Arctic Urals). Russ Geol Geophys 57:1419–1436

Shimizu Y, Arai S, Morishita T, Ishida Y (2008) Origin and significance of spinel-pyroxene symplectite in lherzolite xenoliths fromTallante, SE Spain. Mineral Petrol 94:27–43

Spray JG (1988) Generation and crystallization of an amphibolite shear melt: an investigation using radial friction welding apparatus. Contrib Miner Petrol 99:464–475

Spray JG (1992) A physical basis for the frictional melting of some rock-forming minerals. Tectonophysics 204:205–221

Tamura A, Morishita T, Ishimaru S, Hara K, Sanfilippo A, Arai S (2016) Compositional variations in spinel-hosted pargasite inclusions in the olivine-rich rock from the oceanic crust–mantle boundary zone. Contrib Miner Petrol 171:39. https://doi.org/10.1007/s00410-016-1245-9

Ullah Z, Li J-W, Robinson PT, Wu W-W, Khan A, Dac NX, Abdalla Adam MM (2020) Mineralogy and geochemistry of peridotites and chromitites in the Jijal Complex ophiolite along the Main Mantle Thrust (MMT or Indus Suture Zone) North Pakistan. Lithos 366–367:105566. https://doi.org/10.1016/j.lithos.2020.105566

Van Duysen JC, Doukhan N, Doukhan JC (1985) Transmission electron microscope study of dislocations in orthopyroxene (Mg, Fe)$_2$Si$_2$O$_6$. Phys Chem Miner 12:39–44

Wells PRA (1977) Pyroxene thermometry in simple and complex systems. Contrib Miner Petrol 62:129–139

Wood BJ, Banno S (1973) Garnet-orthopyroxene and orthopyroxene-clinopyroxene relationships in simple and complex systems. Contrib Miner Petrol 42:109–124

Xiong F, Zoheir B, Robinson PT, Yang J, Xu X, Meng F (2020) Genesis of the Ray-Iz chromitite, Polar Urals: Inferences to mantle conditions and recycling processes. Lithos 374–375:105699. https://doi.org/10.1016/j.lithos.2020.105699

Yamamoto J, Ando J, Kagi H, Inoue T, Yamada A, Yamazaki D, Irifune T (2008) In situ strength measurements on natural upper-mantle minerals. Phys Chem Miner 35:249–257. https://doi.org/10.1007/s00269-008-0218-6

Yudovskaya MA, Costin G, Shilovskikh VV, Chaplygin I, McCreesh M, Kinnaird J (2019) Bushveld symplectic and sieve textured chromite is a result of coupled dissolution-reprecipitation: a comparison with xenocrystic chromite reactions in arc basalt. Contrib Miner Petrol 174:74. https://doi.org/10.1007/s00410-019-1613-3

Zhou MF, Robinson PT, Bai WJ (1994) Formation of podiform chromites by melt/rock interaction in the upper mantle. Miner Deposita 29:98–101

Zhou M-F, Robinson PT, Malpas J, Li Z (1996) Podiform chromitites in the Luobusa ophiolite (Southern Tibet): Implications for melt-rock Interaction and chromite segregation in the upper mantle. J Petrol 37:3–21